

Spatiotemporal dynamics of models for microtubule polymerization

Martin Hammele^{1,2} and Walter Zimmermann¹

¹*Theoretische Physik, Universität Bayreuth, D-95440 Bayreuth, Germany*

²*Theoretische Physik, Universität des Saarlandes, D-66041 Saarbrücken, Germany*

(Dated: February 27, 2008)

The polymerization of microtubules becomes oscillatory under certain conditions and in experiments it gives rise to spatially inhomogeneous patterns. The oscillatory microtubule polymerization has been attributed to a Hopf bifurcation by using reduced models for the biochemical reaction cycle [M. Hammele and W. Zimmermann Phys. Rev. E **67**, 021903 (2003)]. These previously introduced models for a homogeneous polymerization are extended by taking into account spatial degrees of freedom and a global conservation condition of tubulin dimers. Close to the threshold of the Hopf bifurcation, we reduce the basic model equations of the biochemical reaction cycle by a perturbation analysis to a complex Ginzburg-Landau equation. In terms of this equation we indeed find for a large range of parameters spatially inhomogeneous polymerization patterns which often behave spatiotemporally chaotic. Numerical simulations of the basic model equations confirm these analytical predictions. Moreover, further beyond the threshold of the Hopf bifurcation, beyond a secondary threshold, spatially homogeneous oscillations, which are unstable immediately above threshold, are stable. In this regime also long lasting and interesting spatially anharmonic transients are predicted.

PACS numbers: Valid PACS appear here

I. INTRODUCTION

Microtubules are rather long and rigid cylindrical filaments which are ubiquitous in eukaryotic cells [1–3]. They are made of the dimer forming proteins α and β tubulin and represent one of the three major classes of filaments in the cytoplasm of cells, which play an important role for several cell functions, such as the maintenance of the cell shape, cell division, etc. Mechanical work in cells is performed by microtubule polymerization [4] and microtubules are also involved in intracellular transport by serving as transport rails for molecular motors such as dynein and kinesin [1–3].

The polymerization of single microtubules already exhibits a complex and for the cell function important dynamics [5, 6]. Collective phenomena of many microtubules are also known, such as the inherent propensity to generate an oscillatory behavior of the density of microtubule filaments during their polymerization [7–20], whereby this polymerization may become spatially inhomogeneous as described in Ref. [12]. Further self-organization phenomena lead to stationary and spatially periodic patterns and some of them are sensitive to the gravitational field [21–23], whereby the induced patterns may have their origin in the buckling of filament bundles [24]. The interaction between filaments and motor proteins leads in addition to pattern formation [25–30], as well as the interplay of the nematic ordering of filaments with the kinetics of microtubule polymerization [31].

In the presence of GTP (guanosine triphosphate), microtubules nucleate and polymerize to long rigid filaments. They are highly dynamic and may spontaneously change on the time scale of minutes via a so-called *catastrophe* from a growing to a shrinking state or via a so-called *rescue* from a shrinking to a growing state. This switching between the growing and shrinking phases

takes place randomly. It has been observed both *in vivo* and *in vitro* [32–35] and it has been called *dynamical instability* [32, 33]. Microtubules are formed in a cell at nucleation sites or, *in vitro*, the nucleation may take place spontaneously in the case of high tubulin concentrations. Tubulin-*t*, i.e. tubulin liganded with GTP, promotes the formation and growth of microtubules, whereas tubulin-*d*, i.e. tubulin liganded with GDP (guanosine diphosphate) being released during the microtubule depolymerization, inhibits their formation and growth. The complete biochemical reaction cycle is irreversible, so the polymerization process slows down during the transformation of tubulin-*t* dimers to tubulin-*d* dimers. However, in the presence of an enzymatic regeneration system, the tubulin-*d* may be regenerated into tubulin-*t* by an exchange of its GDP unit for GTP and the nonequilibrium process of the whole cycle of microtubule polymerization may be maintained over a long time [21].

During the last decades pattern formation in dissipative and spatially extended systems has attracted considerable interest [36–39], including spatiotemporal structures during oscillatory chemical reactions [40], such as the famous Belousov-Zhabotinsky reaction [41]. In contrast to common reaction-diffusion systems, microtubules may undergo an experimentally observed orientational ordering transition beyond a critical filament density [42]. In the range of the oscillatory microtubule polymerization, this orientational ordering may give rise to interesting phenomena which have not been addressed yet. This potential makes the system, besides its significance for biological functions, also to an attractive model system for studies about pattern formation far from thermal equilibrium.

The effects of spatial degrees of freedom on the oscillatory microtubule polymerization are rather unexplored. Two models, which have been analyzed in Ref. [20] with-

out spatial degrees of freedom, are extended in this work by taking into account the diffusion of tubulin dimers and of microtubules. Both models cover major reaction steps of the polymerization/depolymerization process and they also capture the length distribution of the filaments. The two models show a Hopf bifurcation to an oscillatory microtubule polymerization, if the initial concentration of the tubulin dimers exceeds a certain critical value [20]. Since tubulin dimers are neither created nor annihilated, the overall amount of tubulin dimers is conserved. This constraint results in an additional equation for the local density of dimers, including the density of the two kinds of free dimers as well as the tubulin dimers incorporated into microtubules or oligomers. The respective differential equation resembles a continuity equation and renders the modeling rather different from the spatially homogeneous case [20].

The two dimensional spatial patterns observed experimentally for microtubule polymerization in Ref. [12] give rise to the interesting question whether a spatially homogeneous and temporal oscillating microtubule polymerization, as considered in the absence of spatial degrees of freedom in a previous work [20], is stable or unstable with respect to spatially inhomogeneous modulations. Hence, the respective stability properties of the nonlinear solutions are analyzed in terms of a common and rather efficient approach, where the basic model equations are reduced to a so-called amplitude equation or Ginzburg–Landau equation by a multiple scale perturbation technique close to the Hopf bifurcation [39]. This amplitude equation covers the spatiotemporal dynamics close to the threshold of a supercritical bifurcation. Therefore, if the coefficients of this equation are known in terms of the model parameters, a major part of the exploration of the nonlinear solutions can be performed analytically or by simulations of the single amplitude equation. The validity range of the amplitude equation beyond the threshold of the Hopf bifurcation is not known a priori for a specific system; it is estimated in this work by comparing its solution behavior with numerical solutions of the full model equations.

In Sec. II we briefly describe the main reaction steps of the microtubule polymerization and extend the two models introduced in Ref. [20], called model I and model II, by spatial degrees of freedom. The stability of the stationary and homogeneous solutions, as summarized in Sec. III, is investigated in Sec. IV. The so-called amplitude equation of the oscillatory solution is derived in Sec. V, where we explore its solution behaviour also in terms of the kinetic reaction parameters. In Sec. VI we present a few selected numerical results of the full reaction equations. The technical details of the numerical scheme, capturing also the conservation of the initial tubulin concentration, are given in the Appendix. A summary and some concluding remarks are given in Sec. VII.

II. MODELS FOR MICROTUBULE POLYMERIZATION

Two models describing the spatially homogeneous microtubule polymerization, introduced in Ref. [20] and references therein, are extended by spatial degrees of freedom in order to describe also inhomogeneous processes. At high concentrations of GTP liganded tubulin dimers $c_t(\mathbf{r}, t)$, the so-called tubulin- t , microtubules may spontaneously nucleate to small clusters of $\alpha - \beta$ tubulin dimers which polymerize further to long cylindrical rigid fibers. The growth velocity of polymerizing microtubules, v_g , is sensitive to temperature variations, but v_g is rather independent of the density c_t [5, 43]. Growing microtubules may change via a so-called *catastrophe* with a transition rate f_{cat} from their growing to a rapidly depolymerizing state, whereby the shrinking velocity v_s is much larger than the growing one, $v_s \gg v_g$. During the depolymerization of microtubules they may be either fragmented into oligomers as described by the density $c_{oli}(\mathbf{r}, t)$ or directly into GDP liganded tubulin dimers of the density $c_d(\mathbf{r}, t)$, the so-called tubulin- d dimers. Oligomers are stabilized by GDP and destabilized by GTP [10, 44] and in the latter case they are fragmented further into tubulin- d dimers.

By activating an enzymatic process, tubulin- d can be regenerated into tubulin- t due to an exchange of a GDP for a GTP unit as long as sufficient GTP is available. In this case the whole microtubule polymerization cycle may be maintained over several hours, i.e. over many periods of the oscillating microtubule polymerization. In which manner the various reaction rates of the polymerization cycle are determined by the concentration of c_t depends on the respective experiment.

A number of models, as for instance described in Ref. [16], take into account many reaction steps in great detail. Here, we will especially focus on a few rate limiting steps of the polymerization cycle, such as the nucleation, the growth and the decay of microtubules as well as the regeneration of tubulin- d to tubulin- t dimers. Due to the *dynamical instability* of microtubules, one may also expect a transition from the shrinking microtubules back to the growing ones, which is often described by a so-called *rescue* rate. This rate is in many cases rather small compared to the catastrophe rate and will therefore be neglected throughout this work. As an intermediate step between the growing microtubules and the final product of the cascade of microtubule decay, the tubulin- d dimers, we take further into account either the dynamics of shrinking microtubules in model I or the decay dynamics of oligomers in model II. One of both rate limiting factors is already sufficient for an oscillatory microtubule polymerization. These two simplified reaction schemes are sketched in Ref. [20] and the effects of spatial degrees of freedom are analyzed in detail in the rest of this work.

A. Dynamics of growing microtubules

The number of growing microtubule filaments of length l in a unit volume at a site \mathbf{r} and at the time t is described by the length-dependent filament density $p_g(\mathbf{r}, t, l)$, which obeys the partial differential equation

$$\partial_t p_g = -f_{cat} p_g - v_g \partial_l p_g + D_p \Delta p_g. \quad (1)$$

The first term describes the decay of growing microtubules, either into shrinking ones (model I) or into oligomers (model II), and the second term governs the growth of filaments with velocity v_g , which we assume to be constant throughout this work. The diffusion of microtubules is covered by the last term with the diffusion constant $D_p(l)$, which is different parallel or perpendicular to the filament orientation [45]. It is, however, in both directions much smaller than the diffusion constant D_c of the tubulin dimers. Accordingly, we will neglect for the sake of simplicity in most cases the filament diffusion, i.e. $D_p = 0$.

1. Catastrophe rate and boundary condition

Similar to previous models about oscillatory microtubule polymerization [5, 6, 13, 20], we choose a c_t -dependent catastrophe rate of the form

$$f_{cat}(c_t) = f e^{-c_t/c_f} \quad (2)$$

with an amplitude f and a typical decay constant c_f . The evolution equation (1) is of first order with respect to the filament length l and for its boundary condition we choose as previously [20]:

$$p_g(\mathbf{r}, l = 0, t) = \frac{\nu}{v_g}. \quad (3)$$

The nucleation rate ν may depend on the initial concentration c_0 of tubulin dimers, but it is rather independent of the dynamics of $c_t(t)$ [43, 46]. Here, we assume a constant nucleation rate throughout the work.

B. Conservation of tubulin in a spatially extended system

The total amount of tubulin dimers in a spatially extended system is conserved during the polymerization/depolymerization cycle, i.e. tubulin dimers are neither created nor annihilated. This may be expressed by a local conservation law for the density $n(\mathbf{r}, t)$ which is for model I composed of the local dimer densities $c_t(\mathbf{r}, t)$ and $c_d(\mathbf{r}, t)$ as well as of the growing and shrinking microtubules $p_g(\mathbf{r}, l, t)$ and $p_s(\mathbf{r}, l, t)$, respectively. In the case of model II, one has to substitute the density of the shrinking microtubules for the oligomer density $c_{oli}(\mathbf{r}, t)$. The local density $n(\mathbf{r}, t)$ obeys the conservation law

$$\partial_t n(\mathbf{r}, t) = -\nabla \cdot \mathbf{j}(\mathbf{r}, t), \quad (4)$$

where the current density $\mathbf{j}(\mathbf{r}, t)$ depends on the model under investigation. Its specific form is presented for model I in Sec. II C and for model II in Sec. II D. The integral

$$\frac{1}{V} \int_V d^3 \mathbf{r} n(\mathbf{r}, t = 0) = c_0 \quad (5)$$

gives the density of tubulin dimers, c_0 , independent of the phase of the polymerization cycle. The overall density c_0 may be fixed by the initial preparation (condition) in the respective experiment. Integrating Eq. (4) and using Gaussian's law for the specific case of a vanishing net flux through the surface O of the volume V , i.e.

$$\int_O d\mathbf{f} \cdot \mathbf{j}(\mathbf{r}, t) = 0, \quad (6)$$

one gets

$$\frac{1}{V} \frac{d}{dt} \int_V d^3 \mathbf{r} n(\mathbf{r}, t) = 0. \quad (7)$$

The boundary condition in Eq. (6) may be satisfied by applying, for instance, no-flux or spatially periodic boundary conditions. The overall density c_0 in Eq. (5) is then due to Eq. (6) preserved.

C. Model I includes the dynamics of shrinking microtubules

Here, the dynamics of shrinking microtubules, described by the length-dependent distribution function $p_s(\mathbf{r}, t, l)$,

$$\partial_t p_s = f_{cat} p_g + v_s \partial_l p_s + D_p \Delta p_s, \quad (8)$$

is taken into account as an intermediate state between growing microtubules and tubulin- d dimers. The catastrophe rate f_{cat} describes the transition from growing to shrinking microtubules, v_s is the shrinking velocity and for the diffusion constant D_p we use the same value as for the growing microtubules in Eq. (1). Since the diffusion of microtubules is rather slow compared to the tubulin dimers, $D_p \ll D_c$, D_p will be neglected in many cases. The boundary condition with respect to the length of shrinking microtubules is

$$p_s(\mathbf{r}, l \rightarrow \infty, t) = 0, \quad (9)$$

because, due to the decay rate f_{cat} , no growing microtubules are left at large values of l serving as a source for $p_s(l \rightarrow \infty)$.

The dynamical equations for tubulin- t dimers, $c_t(\mathbf{r}, t)$, and tubulin- d dimers, $c_d(\mathbf{r}, t)$, are given by

$$\partial_t c_t = -\gamma v_g \int_0^\infty dl p_g + \alpha c_d + D_c \Delta c_t, \quad (10a)$$

$$\partial_t c_d = \gamma v_s \int_0^\infty dl p_s - \alpha c_d + D_c \Delta c_d, \quad (10b)$$

where we have assumed the same diffusion constant D_c for $c_t(\mathbf{r}, t)$ and $c_d(\mathbf{r}, t)$. The consumption of tubulin- t during the growth of microtubules is described by the first term in Eq. (10a), where γ is a length factor describing the number of tubulin dimers incorporated into a unit length of microtubules. The inactive tubulin- d dimers being released by the shrinking microtubules are described by the first term in Eq. (10b), and they are regenerated into their active form, c_t , with a constant rate α . This regeneration process is the persistent energy supply of the biochemical reaction cycle that keeps the system far from thermal equilibrium.

For model I, the whole dimer density $n(\mathbf{r}, t)$ at site \mathbf{r} and time t is given by

$$n(\mathbf{r}, t) = c_t(\mathbf{r}, t) + c_d(\mathbf{r}, t) + \gamma L(\mathbf{r}, t), \quad (11)$$

and the related dimer current $\mathbf{j}(\mathbf{r}, t)$ is proportional to the local density gradients

$$\mathbf{j}(\mathbf{r}, t) = -D_c \nabla (c_t + c_d) - D_p \gamma \nabla L, \quad (12)$$

where the overall length of microtubules per unit volume

$$L(\mathbf{r}, t) = \int_0^\infty dl l [p_g(\mathbf{r}, l, t) + p_s(\mathbf{r}, l, t)] \quad (13)$$

has been introduced. Equation (11) together with Eq. (12) provides according to Eq. (4) the following equation of motion for the density $n(\mathbf{r}, t)$:

$$\partial_t n = D_c \Delta (c_t + c_d) + D_p \gamma \Delta L. \quad (14)$$

In addition, using the expression given by Eq. (11), we can eliminate the tubulin- d concentration in Eqs. (10a) and (14), and we obtain the two governing equations for c_t and n

$$\begin{aligned} \partial_t c_t &= -\gamma \int_0^\infty dl [v_g p_g + \alpha l (p_g + p_s)] \\ &\quad + \alpha (n - c_t) + D_c \Delta c_t, \end{aligned} \quad (15a)$$

$$\partial_t n = D_c \Delta n + \gamma (D_p - D_c) \Delta L. \quad (15b)$$

Equation (10b) is then always fulfilled and model I is described by Eq. (1), Eq. (8) and Eqs. (15).

D. Model II includes the dynamics of oligomers

Besides shrinking microtubules, a further intermediate product in the cascade of decaying microtubules are oligomers which are composed of several tubulin dimers. Instead of the shrinking velocity v_s of microtubules, also the decay dynamics of oligomers can be a rate limiting step of the reaction cycle [9, 44]. Accordingly, we replace in model II the dynamical equation for $p_s(t, \mathbf{r}, l)$ by a dynamical equation for the density of oligomers, $c_{oli}(\mathbf{r}, t)$, which is coupled to the dynamics of tubulin- d dimers as follows:

$$\partial_t c_{oli} = \eta f_{cat} \int_0^\infty dl l p_g - \chi c_{oli} + D_{oli} \Delta c_{oli}, \quad (16a)$$

$$\partial_t c_d = \chi \lambda c_{oli} - \alpha c_d + D_c \Delta c_d. \quad (16b)$$

Here, the catastrophe rate f_{cat} , as given in Eq. (2), describes the decay of growing microtubules into oligomers, which dissociate themselves into tubulin- d dimers by the rate χ and build a source term in the equation of motion (16b). D_{oli} denotes the diffusion constant of the oligomers, η measures the number of oligomers per unit length of the microtubules and λ is a measure for the number of tubulin dimers per oligomer. As for model I, the tubulin- d dimers are regenerated into tubulin- t dimers by the rate α in order to close the reaction cycle. The equation of motion for the growing microtubules p_g is the same as for model I, cf. Eq. (1), but in the equation of motion for c_t given in Eq. (10a), we have to substitute the length factor γ for the product $\eta \lambda$. Since oligomers are much larger than tubulin- d dimers and microtubules are even larger than oligomers, one has for the various diffusion constants a hierarchy as follows: $D_c \gg D_{oli} \gg D_p$.

We again use Eq. (3) with a spatially constant nucleation rate ν as a boundary condition for the growing microtubules with respect to their length l .

The mean length of growing microtubules is given by the integral over the length distribution,

$$L(\mathbf{r}, t) = \int_0^\infty dl l p_g(\mathbf{r}, l, t), \quad (17)$$

and, therefore, the overall density of tubulin dimers for model II at site \mathbf{r} and time t is given by

$$n(\mathbf{r}, t) = c_t(\mathbf{r}, t) + c_d(\mathbf{r}, t) + \lambda c_{oli}(\mathbf{r}, t) + \eta \lambda L(\mathbf{r}, t). \quad (18)$$

The associated dimer current is

$$\mathbf{j} = -D_c \nabla (c_t + c_d) - D_{oli} \lambda \nabla c_{oli} - D_p \eta \lambda \nabla L. \quad (19)$$

Again, the last term in Eq. (19) describes the current that stems from the polymerized tubulin dimers, which may locally change the dimer density $n(\mathbf{r}, t)$. According to Eq. (4), one obtains the following equation of motion for the density n :

$$\partial_t n = D_c \Delta (c_t + c_d) + D_{oli} \lambda \Delta c_{oli} + D_p \eta \lambda \Delta L. \quad (20)$$

Using Eq. (18), we can eliminate in Eq. (16b) and Eq. (20) the density of the oligomers c_{oli} . Therefore, instead of the dynamics of oligomers, the dynamics of the density $n(\mathbf{r}, t)$ is considered and we obtain besides the dynamical equations for p_g and c_t the two coupled equations

$$\begin{aligned} \partial_t c_d &= D_c \Delta c_d + \chi \left(n - c_t - c_d - \eta \lambda \int_0^\infty dl l p_g \right) \\ &\quad - \alpha c_d, \end{aligned} \quad (21a)$$

$$\begin{aligned} \partial_t n &= (D_c - D_{oli}) \Delta (c_t + c_d) + D_{oli} \Delta n \\ &\quad + (D_p - D_{oli}) \eta \lambda \Delta L. \end{aligned} \quad (21b)$$

Accordingly, Eqs. (1), (10a) and (21) describe the whole polymerization cycle for model II, involving oligomers as an intermediate decay product of microtubules. In addition, the conservation of the total amount of tubulin dimers is explicitly taken into account via Eqs. (19) and (20) together with the boundary condition in Eq. (6).

III. STATIONARY, HOMOGENEOUS SOLUTIONS

The stationary and spatially uniform solutions of the model equations introduced in Sec. II agree with those presented in Ref. [20] and we briefly summarize some results here. Equations (1) and (8) are first-order linear differential equations with respect to the length l . Hence, in the stationary and spatially homogeneous case, they have exponentially decaying solutions

$$p_{g,s}^{(0)}(l) = \frac{\nu}{v_{g,s}} \exp\left(-\frac{f_{cat}^{(0)}}{v_g} l\right), \quad (22)$$

where $f_{cat}^{(0)} = f \exp(-c_t^{(0)}/c_f)$ and $c_t^{(0)}$ represent the stationary and homogeneous values of the catastrophe rate and tubulin- t density, respectively.

For model I, the density $c_t^{(0)}$ itself is determined by the nonlinear equation

$$c_0 - c_t^{(0)} = \frac{\nu\gamma v_g}{f_{cat}^{(0)}} \left(\frac{1}{\alpha} + \frac{1}{f_{cat}^{(0)}}(1 + \beta) \right), \quad (23)$$

which follows from Eq. (15a) with $n^{(0)} = c_0$, being in agreement with the conservation law in Eq. (5). In Eq. (23) the velocity ratio $\beta = v_g/v_s$ has been introduced. The corresponding tubulin- d density $c_d^{(0)}$ can be calculated via Eq. (10b).

For model II, a similar nonlinear equation for the determination of $c_t^{(0)}$ can be derived

$$c_0 - c_t^{(0)} = \frac{\nu\eta\lambda v_g}{f_{cat}^{(0)}} \left(\frac{1}{\alpha} + \frac{1}{\chi} + \frac{1}{f_{cat}^{(0)}} \right), \quad (24)$$

which follows from Eq. (21a). The densities of the oligomers and tubulin- d dimers may be determined via Eqs. (16). For various limiting cases analytical expressions for $c_t^{(0)}$ can be derived which give some additional insight about its dependence on various parameters, as described in Ref. [20].

IV. THRESHOLD OF THE HOPF BIFURCATION

Beyond a critical initial concentration of tubulin dimers, c_{0c} , as defined below, the stationary state of the respective microtubule polymerization cycle given in Sec. III becomes oscillatory in time via a supercritical Hopf bifurcation, as described for the spatially homogeneous case in Ref. [20]. Here, we extend this analysis by investigating the influence of spatial degrees of freedom on the linear as well as nonlinear properties of the Hopf bifurcation described by the model equations presented in Sec. II. For the sake of simplicity, we restrict our analysis to one spatial dimension and we discard orientational ordering effects of the filaments. The

threshold of the Hopf bifurcation is calculated by deriving linear equations of motion for small inhomogeneous perturbations with respect to the stationary and homogeneous basic state which have solutions proportional to $\propto \exp(\sigma t + iqx)$. For an initial concentration c_0 corresponding to $\text{Re}(\sigma) > 0$, the perturbations grow exponentially in time and the uniform solutions become unstable. Otherwise, i.e. $\text{Re}(\sigma) < 0$, the stationary reaction cycle remains stable. The *neutral stability condition* $\text{Re}[\sigma(q)] = 0$ determines for varying wave numbers q the initial concentration $c_0(q)$ at the so-called *neutral curve*, which separates the stable from the unstable parameter range, while the expression $\text{Im}[\sigma(q)] = \omega_0(q)$ provides the frequency along that curve. The minimum of the neutral curve gives the critical initial concentration $c_{0c} = c_0(q = q_c) = \min[c_0(q)]$ at the critical wave number q_c and the corresponding Hopf frequency is given by $\omega_c = \omega_0(q = q_c)$.

A. Model I

The stability of the stationary reaction cycle of model I, as described by $p_{g,s}^{(0)}, n^{(0)}$ and $c_t^{(0)}$, with respect to small deviations $p_{g,s}^{(1)}, n^{(1)}$ and $c_t^{(1)}$ is determined. For this purpose, the ansatz

$$\begin{aligned} p_{g,s} &= p_{g,s}^{(0)} + p_{g,s}^{(1)}(x, l, t), & c_t &= c_t^{(0)} + c_t^{(1)}(x, t), \\ n &= n^{(0)} + n^{(1)}(x, t) \end{aligned} \quad (25)$$

is chosen and a linearization of the governing equations (1),(8) and (15) results in a set of linear equations with constant coefficients describing the dynamics of the small perturbations:

$$\begin{aligned} \partial_t p_g^{(1)} &= -p_g^{(0)} f_{cat}^{(1)} - \left(f_{cat}^{(0)} + v_g \partial_l \right) p_g^{(1)} \\ &\quad + D_p \partial_x^2 p_g^{(1)}, \end{aligned} \quad (26a)$$

$$\begin{aligned} \partial_t p_s^{(1)} &= p_g^{(0)} f_{cat}^{(1)} + f_{cat}^{(0)} p_g^{(1)} + v_s \partial_l p_s^{(1)} \\ &\quad + D_p \partial_x^2 p_s^{(1)}, \end{aligned} \quad (26b)$$

$$\begin{aligned} \partial_t c_t^{(1)} &= -\gamma \int_0^\infty dl [v_g p_g^{(1)} + \alpha l (p_g^{(1)} + p_s^{(1)})] \\ &\quad + \alpha (n^{(1)} - c_t^{(1)}) + D_c \partial_x^2 c_t^{(1)}, \end{aligned} \quad (26c)$$

$$\begin{aligned} \partial_t n^{(1)} &= \gamma (D_p - D_c) \partial_x^2 \int_0^\infty dl l (p_g^{(1)} + p_s^{(1)}) \\ &\quad + D_c \partial_x^2 n^{(1)}. \end{aligned} \quad (26d)$$

Here, $f_{cat}^{(1)}$ denotes the first-order correction of an expansion of the catastrophe rate $f_{cat} = f_{cat}^{(0)} + f_{cat}^{(1)} + \dots$ with respect to c_t . It is given by

$$f_{cat}^{(1)} = -f_{cat}^{(0)} \frac{c_t^{(1)}}{c_f}. \quad (27)$$

We assume spatially periodic boundary conditions and since Eqs. (26) are first-order differential equations with

respect to time, we choose the following Fourier ansatz for the two perturbations $c_t^{(1)}$ and $n^{(1)}$:

$$\begin{aligned} c_t^{(1)} &= A e^{\sigma t + i q x} + \text{c.c.}, \\ n^{(1)} &= A_n e^{\sigma t + i q x} + \text{c.c.}, \end{aligned} \quad (28)$$

(c.c. stands for the complex conjugate). Here q denotes the perturbation wave number and σ is a complex parameter, which is determined as outlined in the following. After inserting the respective expressions for $c_t^{(1)}$ and $f_{cat}^{(1)}$ in Eqs. (26a) and (26b), one may easily integrate the latter ones with respect to the length l of the microtubules. After a few intermediate steps, the following expressions for $p_g^{(1)}$ and $p_s^{(1)}$ are obtained:

$$\begin{aligned} p_g^{(1)} &= -\frac{\nu f_{cat}^{(0)} A}{v_g c_f (\sigma + D_p q^2)} \exp\left(\sigma t - \frac{f_{cat}^{(0)}}{v_g} l\right) \\ &\times \left[\exp\left(-\frac{(\sigma + D_p q^2) l}{v_g}\right) - 1 \right] \exp(i q x) + \text{c.c.}, \end{aligned} \quad (29a)$$

$$\begin{aligned} p_s^{(1)} &= -\frac{\nu f_{cat}^{(0)} A}{v_s c_f (\sigma + D_p q^2)} \exp\left(\sigma t - \frac{f_{cat}^{(0)}}{v_g} l\right) \\ &\times \left[c_1 \exp\left(-\frac{(\sigma + D_p q^2) l}{v_g}\right) + c_2 \right] \exp(i q x) + \text{c.c.}, \end{aligned} \quad (29b)$$

with the two complex coefficients

$$\begin{aligned} c_1 &= \frac{f_{cat}^{(0)}}{f_{cat}^{(0)} + (1 + \beta)(\sigma + D_p q^2)}, \\ c_2 &= \frac{\sigma + D_p q^2 - f_{cat}^{(0)}}{f_{cat}^{(0)} + \beta(\sigma + D_p q^2)}. \end{aligned} \quad (30)$$

With the help of the expression for $p_g^{(1)}$ in Eq. (29a), the integrals $\int dl p_g^{(1)}$ and $\int dl l p_g^{(1)}$ occurring in Eqs. (26c) and (26d) can be explicitly evaluated

$$\int_0^\infty dl p_g^{(1)} = \frac{\nu A}{c_f} k_1 e^{\sigma t + i q x} + \text{c.c.}, \quad (31a)$$

$$\int_0^\infty dl l p_g^{(1)} = \frac{\nu v_g A}{c_f} k_2 e^{\sigma t + i q x} + \text{c.c.}, \quad (31b)$$

where the two abbreviations

$$\begin{aligned} k_1 &= \frac{1}{f_{cat}^{(0)} + \sigma + D_p q^2}, \\ k_2 &= \frac{\sigma + D_p q^2 + 2f_{cat}^{(0)}}{f_{cat}^{(0)} \left(f_{cat}^{(0)} + \sigma + D_p q^2 \right)^2}, \end{aligned} \quad (32)$$

have been introduced. For the integral $\int dl l p_s^{(1)}$ one obtains

$$\int_0^\infty dl l p_s^{(1)} = -\frac{\nu v_g^2 A}{v_s c_f} b_1 e^{\sigma t + i q x} + \text{c.c.} \quad (33)$$

with the complex coefficient

$$b_1 = \frac{c_1 f_{cat}^{(0)2} + c_2 \left(\sigma + D_p q^2 + f_{cat}^{(0)} \right)^2}{f_{cat}^{(0)} (\sigma + D_p q^2) \left(f_{cat}^{(0)} + \sigma + D_p q^2 \right)^2}. \quad (34)$$

After inserting the respective integrals in Eqs. (26c) and (26d), one obtains two coupled linear and homogeneous equations for the amplitudes A and A_n , which may be written in matrix form

$$\mathcal{M} \mathbf{u}_e = \mathbf{0}, \quad (35)$$

with the coefficient matrix

$$\mathcal{M} = \begin{pmatrix} G(\sigma + \alpha + D_c q^2) + k_1 + \alpha \varkappa & -G\alpha \\ (D_p - D_c) \varkappa q^2 & G(\sigma + D_c q^2) \end{pmatrix}, \quad (36)$$

the vector $\mathbf{u}_e = (A, A_n)$, as well the abbreviations $\varkappa = k_2 - \beta b_1$ and $G = c_f / (\gamma \nu v_g)$. Equation (35) only admits nontrivial solutions if the determinant of the matrix \mathcal{M} vanishes, i.e. $\det(\mathcal{M}) = 0$. The latter condition leads to a polynomial of fifth-order in σ with rather lengthy coefficients, which are not given here. The solutions of this polynomial provide the dispersion relation $\sigma(q)$ for model I, which depends on the kinetic parameters α, ν, β as well as on the diffusion constants D_p and D_c , respectively. Decomposing the dispersion relation into its real and imaginary part yields the growth rate $\text{Re}[\sigma(q)]$ and the corresponding frequency $\omega(q) = \text{Im}[\sigma(q)]$ of the Hopf bifurcation as functions of the wave number q . Assuming neutral stability, $\text{Re}[\sigma(q)] = 0$, provides a condition for the determination of the neutral curve, $c_0(q)$, which separates as a function of the wave number q the exponentially decaying perturbations from the growing ones. The minimum of this neutral curve determines the critical initial concentration c_{0c} .

B. Model II

Following model I, we analyze the dynamics of small perturbations with respect to the stationary and homogeneous basic state $p_g^{(0)}, c_{t,d}^{(0)}$ and $n^{(0)}$ of the reaction cycle of model II. Using the separation ansatz

$$\begin{aligned} p_g &= p_g^{(0)} + p_g^{(1)}(x, l, t), & c_{t,d} &= c_{t,d}^{(0)} + c_{t,d}^{(1)}(x, t), \\ n &= n^{(0)} + n^{(1)}(x, t), \end{aligned} \quad (37)$$

and linearizing Eqs. (1), (10a) and (21) with respect to the small perturbations $p_g^{(1)}, c_{t,d}^{(1)}$ and $n^{(1)}$ gives the following set of dynamical equations with constant coefficients

for the perturbations:

$$\partial_t p_g^{(1)} = -p_g^{(0)} f_{cat}^{(1)} - \left(f_{cat}^{(0)} + v_g \partial_l \right) p_g^{(1)} + D_p \partial_x^2 p_g^{(1)}, \quad (38a)$$

$$\partial_t c_t^{(1)} = -\eta \lambda v_g \int_0^\infty dl p_g^{(1)} + \alpha c_d^{(1)} + D_c \partial_x^2 c_t^{(1)}, \quad (38b)$$

$$\partial_t c_d^{(1)} = \chi \left(n^{(1)} - c_t^{(1)} - c_d^{(1)} - \eta \lambda \int_0^\infty dl l p_g^{(1)} \right) + D_c \partial_x^2 c_d^{(1)} - \alpha c_d^{(1)}, \quad (38c)$$

$$\partial_t n^{(1)} = D_{oli} \partial_x^2 n^{(1)} + (D_c - D_{oli}) \partial_x^2 \left(c_t^{(1)} + c_d^{(1)} \right) + (D_p - D_{oli}) \eta \lambda \partial_x^2 \int_0^\infty dl l p_g^{(1)}. \quad (38d)$$

$f_{cat}^{(1)}$ denotes the first-order contribution of an expansion of the catastrophe rate and it is also given by Eq. (27).

The solutions of Eqs. (38) depend exponentially on time and, by assuming spatially periodic boundary conditions, the following ansatz for the small perturbations is obvious:

$$\begin{aligned} c_t^{(1)} &= A e^{\sigma t + i q x} + \text{c.c.}, & c_d^{(1)} &= A_d e^{\sigma t + i q x} + \text{c.c.}, \\ n^{(1)} &= A_n e^{\sigma t + i q x} + \text{c.c.} \end{aligned} \quad (39)$$

Similar to model I, the complex parameter σ is determined via a solvability condition as outlined below. Equation (38a) is identical to Eq. (26a) and its solution is therefore also given by Eq. (29a). Inserting this expression for $p_g^{(1)}$ in Eqs. (38b)-(38d), the emerging integrals with respect to the length l are again given by Eqs. (31), and one finally obtains three linear and homogeneous equations for the amplitudes $\mathbf{u}_e = (A, A_d, A_n)$

$$\begin{pmatrix} G(\sigma + D_c q^2) + k_1 & -G\alpha & 0 \\ \chi(G + k_2) & G(\sigma + D_c q^2 + \chi + \alpha) & -G\chi \\ G(D_c - D_{oli})q^2 + (D_p - D_{oli})q^2 k_2 & G(D_c - D_{oli})q^2 & G(\sigma + D_{oli} q^2) \end{pmatrix} \mathbf{u}_e = \mathbf{0}, \quad (40)$$

with $G = c_f / (\eta \lambda \nu v_g)$. The solvability condition for finite solutions $\mathbf{u}_e \neq 0$ requires that the determinant of the coefficient matrix in Eq. (40) vanishes. This results in a fifth-order complex polynomial in σ , which is rather lengthy and is again not presented here. For a fixed set of parameters of model II and after a decomposition of σ into its real and imaginary part, we obtain two coupled equations determining the growth rate $\text{Re}[\sigma(q)]$ and the frequency $\omega(q) = \text{Im}[\sigma(q)]$ of the Hopf bifurcation as functions of the wave number q . Again, the critical values c_{0c} and ω_c are obtained by applying the neutral stability condition $\text{Re}[\sigma(q)] = 0$ and minimizing the resulting neutral curve $c_0(q)$ with respect to q .

C. Results

Applying the neutral stability condition $\text{Re}[\sigma(q = 0)] = 0$ to Eq. (35) or to Eq. (40), one obtains for the respective model the same parameter dependence of the critical tubulin concentration

$$c_{0c} = c_{0c}(\alpha, \nu, v_g, G, \dots) \quad (41)$$

as well as the same frequency ω_c of the homogeneous Hopf bifurcation as discussed in detail in Ref. [20].

If the wave number q is finite then the critical concentration $c_0(q)$, at which the Hopf bifurcation takes place, is for both models larger than the value of the homogeneous instability c_{0c} in Eq. (41). The bottom part of Fig. 1 illustrates the typical shape of the neutral curve $c_0(q)$ for

model I. Beyond this curve, i.e. for $c_0 > c_0(q)$, the stationary solutions become linearly unstable with respect to small oscillatory perturbations. The wave number dependence of the Hopf frequency $\omega_0(q) = \text{Im}[\sigma(q)]$ along the neutral curve is shown in the upper part in Fig. 1.

In the vicinity of the critical density c_{0c} , the neutral curve may be approximated by the parabolic expression

$$c_0(q) = c_{0c} (1 + \xi_0^2 q^2), \quad (42)$$

where the so-called coherence length ξ_0 depends on the kinetic parameters of the reaction cycle, but it is essentially determined by the largest diffusion constant D_c . Also the frequency dispersion $\omega_0(q)$ along the neutral curve has a parabolic shape near $q = 0$. Both aspects are crucial for the solution behavior in the weakly nonlinear regime as discussed in greater detail in Sec. V. The $\pm q$ symmetry of both curves in Fig. 1 indicates the invariance of the model equations with respect to reflections $x \leftrightarrow -x$.

Since the neutral curve for model I as well as for model II takes its minimum at $q = 0$, one always has a bifurcation from the stationary state into oscillatory but spatially homogeneous solutions. Accordingly, density variations at the threshold c_{0c} are not preferred and therefore, one has $\partial_t n^{(1)} = 0$ in Eqs. (26d) and (38d), respectively. So the critical tubulin concentration c_{0c} is the same as in Ref. [20] and it is determined for model I by Eqs. (26a)-(26c) and for model II by Eqs. (38a)-(38c) with $n^{(1)} = 0$ and $A_n \equiv 0$.

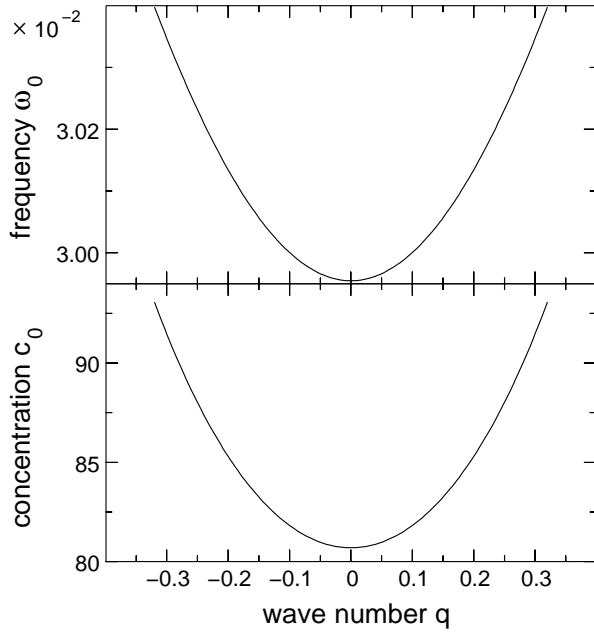


FIG. 1: The neutral curve $c_0(q)$ (lower part) and the Hopf frequency $\omega_0(q)$ (upper part) are shown for model I, where the diffusion constant $D_c = 0.01$ of the tubulin dimers and that of the microtubules $D_p = 0$ has been used. The other parameters are $G = 3000$, $\alpha = \nu = 0.01$, $\beta = 0.1$, $c_f = 3$, and $f = 0.1$. The critical tubulin concentration corresponding to the minimum of the neutral curve is $c_{0c} = 80.69$.

For model II the critical tubulin concentration of the Hopf bifurcation $c_{0c}(\alpha, \chi)$ is shown in Fig. 2 as a function of the regeneration rate α and the oligomer decay rate χ . Beyond this surface the stationary reaction cycle becomes unstable and, moreover, $c_{0c}(\alpha, \chi)$ emphasizes that the Hopf bifurcation is favored at intermediate values of both parameters, whereas large or very small values of them inhibit oscillatory solutions.

For a Hopf bifurcation the fifth-order polynomial obtained from Eq. (35) or Eq. (40) always has two complex conjugate solutions describing the dispersion relation $\sigma(q)$ for the small perturbations. In the neutrally stable case one has $\sigma = \pm i\omega_0$ and hence, apart from $q = 0$, the linear solutions along the neutral curve are superpositions of left and right traveling waves. For the case of equal amplitudes this may lead to a standing wave as given, for instance, for the tubulin- t density by

$$c_t^{(1)} = E \cos(\omega_c t + \varphi) \cos(qx), \quad (43)$$

where E denotes a real amplitude and φ a phase shift. The other densities may be represented in the same way.

V. AMPLITUDE EXPANSION

The threshold of the Hopf bifurcation is unchanged by taking into account spatial degrees of freedom, as shown

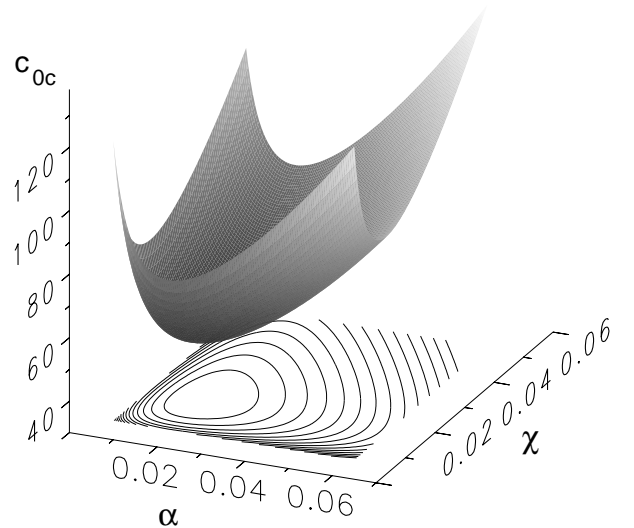


FIG. 2: The critical tubulin concentration c_{0c} is shown for model II as a function of both the regeneration rate α and the dissociation rate χ , leading to a critical surface for the onset of the Hopf bifurcation. Solid lines indicate projections of constant density onto the $\alpha - \chi$ plane. The remaining parameters are $G = 3000$, $v_g = 0.1$ and $\nu = 0.01$.

in the previous section. So the threshold of the homogeneous Hopf bifurcation, as determined in Ref. [20], is lower than for the spatially-dependent, oscillatory solutions. The homogeneous Hopf bifurcation is always supercritical for model I and for model II. Nevertheless, slightly above this threshold, in the so-called weakly nonlinear regime, the spatiotemporal behavior may be significantly changed by the spatial degrees of freedom as shown in this section and in Sec. VI. We will expose that the spatially homogeneous oscillations are unstable in a large parameter range of model I and for all parameters in the case of model II. This remarkable result may be attributed to the competition between the linear frequency dispersion $\omega_0(q)$ (see e.g. top part in Fig. 1) and the nonlinear frequency dispersion and is known as the *Benjamin-Feir resonance* [39, 47–49].

Close to the bifurcation point of a supercritical bifurcation, there is an efficient method available, the amplitude equation approach, in order to determine the stability of the spatially homogeneous oscillatory solutions with respect to inhomogeneous perturbations [39, 47, 49]. The equation for the envelope $A(x, t)$ of the oscillatory solution is obtained by a perturbation calculation of the basic equations given in Sec. II with respect to small oscillation amplitudes. The linear and nonlinear coefficients of the amplitude equation are determined as functions of the rate constants of the reaction cycle and they determine the stability of the spatially homogeneous oscillating solutions as well as of traveling wave solutions of the amplitude equation.

As a small parameter for the perturbation calculation,

we use the relative distance to the threshold

$$\varepsilon = \frac{c_0 - c_{0c}}{c_{0c}}. \quad (44)$$

The complete perturbation scheme is described in detail for the homogeneous model equations in Ref. [20] and further information about the generic method of amplitude equations is found, for instance, in Ref. [39].

According to the \pm symmetry of the oscillatory behavior, the oscillation amplitude increases with the power law $A \sim \sqrt{\varepsilon}$ and therefore close to threshold, the solutions of the basic equations may be expanded with respect to powers of $\sqrt{\varepsilon}$

$$\mathbf{u} = \mathbf{u}^{(0)} + \varepsilon^{1/2} \mathbf{u}^{(1)} + \varepsilon \mathbf{u}^{(2)} + \varepsilon^{3/2} \mathbf{u}^{(3)} + O(\varepsilon^2), \quad (45)$$

where the vector notation $\mathbf{u}^{(j)} = (\tilde{p}_g^{(j)}, \tilde{p}_s^{(j)}, \tilde{c}_t^{(j)}, \tilde{n}^{(j)})$ is used for model I and $\mathbf{u}^{(j)} = (\tilde{p}_g^{(j)}, \tilde{c}_t^{(j)}, \tilde{c}_d^{(j)}, \tilde{n}^{(j)})$ for model II with $j = 0, 1, 2, 3$. It should be noticed that one has the proportionality $\sqrt{\varepsilon} \tilde{c}_t^{(1)} = c_t^{(1)}$, etc. The components of $\mathbf{u}^{(0)}$ describe the stationary microtubule polymerization as given in Sec. III and the components of $\mathbf{u}^{(1)}$ describe the linear oscillatory contribution that may be written at threshold in the following form:

$$\mathbf{u}^{(1)} = B \mathbf{u}_e e^{i\omega_c t} + \text{c.c.}, \quad (46)$$

with a common amplitude B of the vector \mathbf{u}_e . The latter one includes the amplitude ratios between the respective fields, which are given for model I by Eq. (35) and for model II by Eq. (40). Note that we used the relation $A = \sqrt{\varepsilon} B$.

Close to the threshold, one has $\text{Re}(\sigma) \sim \varepsilon \ll 1$ and the linear solution $\mathbf{u}^{(1)} \sim e^{\sigma t}$ grows or decays only by a very small amount during one oscillation period $2\pi/\omega_c$. These two disparate time scales near the threshold, which is the oscillation period ($\propto 2\pi/\omega_c$) and the growth/decay time ($\propto 1/\varepsilon$), may be separated within the perturbation expansion by introducing a slow time scale $T = \varepsilon t$ [39, 49]. The fast time scale is covered by the exponential function $e^{i\omega_c t}$ and the slow variations will be described by a time-dependent amplitude $B(T)$.

The neutral curve of the Hopf bifurcation has its minimum always at the wave number $q = 0$. Therefore close to the threshold, only long-wavelength modulations with $q < \sqrt{\varepsilon}/\xi_0$ [see Eq. (42)] may become supercritical and, similar to the slow time scale, a slow spatial scale $X = \varepsilon^{1/2} x$ is introduced, which is also described by the envelope $B(X, T)$. Altogether, the linear solution near threshold may be written as

$$\mathbf{u}^{(1)}(t, X, T) = B(X, T) \mathbf{u}_e e^{i\omega_c t} + \text{c.c.}, \quad (47)$$

and the aim of the perturbation calculation is to derive an equation of motion for $B(X, T)$. Instead of applying the chain rule of differentiation in order to differentiate the product of time-dependent functions in Eq. (47), one may replace this operation by the following sum: $\partial_t \rightarrow \partial_t + \varepsilon \partial_T$. Here ∂_t acts only on the fast time-dependence

occurring in the exponential function and ∂_T acts only on the amplitude $B(X, T)$. The same holds for the spatial derivative $\partial_x \rightarrow \partial_x + \sqrt{\varepsilon} \partial_X$ [39].

Using these replacements for the derivatives as well as the ε -expansion of \mathbf{u} , the basic equations for both models given in Sec. II can be ordered with respect to powers of $\sqrt{\varepsilon}$, leading to a hierarchy of partial differential equations. The whole procedure for the spatially independent microtubule polymerization is described in greater detail in Ref. [20] and may be canonically extended to the case including slowly spatial variations.

The amplitude equation for $B(X, T)$ follows from a solvability condition for the equations at order $O(\varepsilon^{3/2})$ and it has the following form [39]:

$$\begin{aligned} \tau_0 \partial_T B &= (1 + ia) B + \xi_0^2 (1 + ib) \partial_X^2 B \\ &\quad - g (1 + ic) |B|^2 B. \end{aligned} \quad (48)$$

Here τ_0 is the relaxation time, a is the linear and c the nonlinear frequency shift, and $\xi_0^2 b$ describes the linear frequency dispersion of the oscillations. If the nonlinear coefficient g is positive one has a supercritical bifurcation and for negative values of g a subcritical bifurcation. As shown in Ref. [20], the nonlinear coefficient g is positive for all investigated parameters and the bifurcation to oscillatory solutions always takes place via a supercritical bifurcation. For the coefficients τ_0 , a , ξ_0^2 , b , g and c , one obtains explicit expressions in terms of the reaction constants of the basic model equations, which have been calculated by using computer algebra. The respective formulas are long and therefore they are not presented here. Instead we have plotted the parameter dependence of these coefficients in Fig. 3 for two sets of parameters of model I.

Rescaling time $T = \varepsilon t$, space $X = \varepsilon^{1/2} x$ and the amplitude $A(x, t) = \sqrt{\varepsilon} B(X, T)$ back to their original units, one obtains the common amplitude equation

$$\begin{aligned} \tau_0 \partial_t A &= \varepsilon (1 + ia) A + \xi_0^2 (1 + ib) \partial_x^2 A \\ &\quad - g (1 + ic) |A|^2 A. \end{aligned} \quad (49)$$

The solution space of this universal equation for the envelope of oscillating fields of a Hopf bifurcation has been intensively explored during the last two decades and an overview of this activity is given by a recent review in [47]. Note that Eq. (49) cannot be derived from a Lyapunov functional and it may exhibit spatiotemporal chaotic solutions.

The linear coefficients in Eq. (49) may be determined either by the perturbation procedure or directly from the dispersion relation $\sigma(q)$ of the basic reaction equations. The connection between these two methods becomes obvious by the following reasoning. The solution $A = 0$ of Eq. (49) corresponds to the stationary polymerization (see Sec. III), which is stable in the range $\varepsilon < 0$ against small perturbations of the form $A \propto e^{\sigma t + i q x}$ and unstable in the range $\varepsilon > 0$. Neglecting the cubic nonlinearity in Eq. (49), one obtains with this ansatz for the pertur-

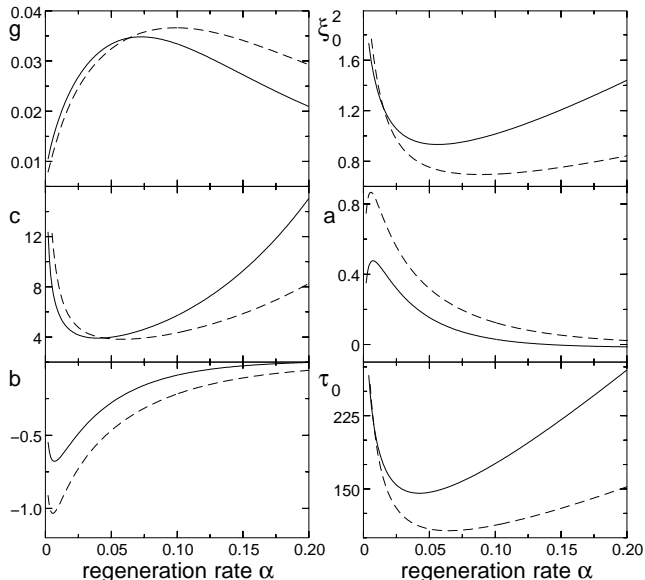


FIG. 3: The linear and nonlinear coefficients of the amplitude equation (49) are shown for model I as functions of the regeneration rate and for two different ratios β between the polymerization and depolymerization velocity: $\beta = 0.1$ (solid line) and $\beta = 0.05$ (dashed line). The rest of parameters are $G = 3000$, $v_g = 0.1$, $\nu = 0.01$, $D_c = 0.01$, and $D_p = 0$.

bations the following dispersion relation:

$$\sigma = \tau_0^{-1} [\varepsilon(1 + ia) - \xi_0^2(1 + ib)q^2]. \quad (50)$$

The complex parameter σ is given in terms of the linear coefficients of the amplitude equation (49). All these linear coefficients may also be expressed in terms of derivatives of σ and c_0 with respect to q or ε (resp. c_0) as follows:

$$\tau_0 = \frac{1}{c_0 c \partial \text{Re}(\sigma) / \partial c_0}, \quad a = c_0 c \tau_0 \frac{\partial \omega}{\partial c_0}, \quad (51a)$$

$$\xi_0^2 = \frac{1}{2c_0 c} \frac{\partial^2 c_0}{\partial q^2}, \quad b = -\frac{\tau_0}{2\xi_0^2} \frac{\partial^2 \omega}{\partial q^2}, \quad (51b)$$

with $\omega = \text{Im}(\sigma)$. The derivatives in Eq. (51a) are evaluated at c_{0c} and the derivatives in Eq. (51b) at $q = 0$. In the neighborhood of the threshold, the dispersion relation $\sigma(q)$ obtained from the amplitude equation (49) agrees with the full dispersion relation given by evaluating the determinant of the matrix in Eq. (36) for model I or in Eq. (40) for model II. Thus, one may determine the linear coefficients τ_0 , a , ξ_0^2 and b directly from the full dispersion relation. However, in order to determine the nonlinear coefficients g and c of the amplitude equation (49) as functions of the rate constants of the polymerization cycle, it is inevitable to carry out the perturbational expansion explicitly.

For model I all coefficients of Eq. (49) are plotted in Fig. 3 as functions of the regeneration rate α and for model II the coefficients ξ_0^2 , b and c are plotted in Fig. 6 as functions of the dissociate rate χ . In addition, in these

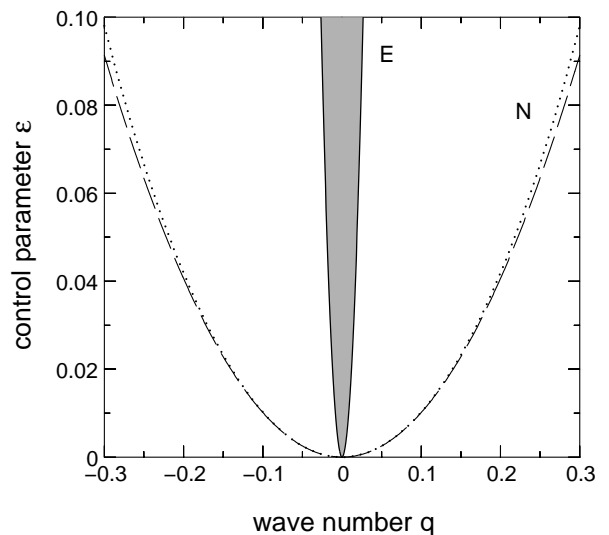


FIG. 4: Neutral curve (dashed line) and Eckhaus stability border (solid line) are shown for model I. The dotted line displays the neutral curve obtained by solving the fully linear stability problem in Eq. (35). The parameters are $\alpha = 0.1$, $\beta = 0.1$, $\nu = 0.01$, $D_c = 0.01$, $D_p = 0$ leading to the following coefficients of the amplitude equation: $b = -0.0895$, $c = 5.713$ and hence $bc = -0.511$. Inside the dark region given by $q < q_E$, traveling waves are stable. The critical tubulin concentration is $c_{0c} = 176.86$ and, for comparison, to the value $\varepsilon = 0.1$, it corresponds an absolute tubulin concentration of $c_0 = 194.55$.

two figures the dependence of the product bc on the parameters α and χ , respectively, is also depicted and, as we will see in the next section, the value of this product determines the stability of the spatially homogeneous oscillations of Eq. (49) and therefore also of the basic equations.

A. Nonlinear wave solutions and their stability

The neutral stability condition $\text{Re}[\sigma(q)] = 0$ applied to Eq. (50) yields the neutral curve $\varepsilon_N = \xi_0^2 q^2$ of the amplitude equation. Above this neutral curve, i.e. for values of the wave number q

$$q^2 < q_N^2 = \frac{\varepsilon_N}{\xi_0^2}, \quad (52)$$

Eq. (49) exhibits traveling wave solutions of the form

$$A = F e^{i(qx + \Omega t)}, \quad (53)$$

where the two unknowns, namely the amplitude F and the frequency Ω , are given as functions of the wave number q by the expressions:

$$F^2 = g^{-1} (\varepsilon - \xi_0^2 q^2), \quad (54)$$

$$\Omega = \tau_0^{-1} (\varepsilon a - \xi_0^2 b q^2 - g c F^2).$$

Note that the amplitude F tends to zero if the wave number q approaches the neutral curve $q \rightarrow q_N$.

However, these traveling wave solutions are only stable with respect to small, inhomogeneous perturbations $v(x, t)$ in a restricted range of the parameters b, c and q [39, 47]. This wave number range may be calculated by using the ansatz

$$A = e^{i(qx + \Omega t)} [F + v(x, t)] \quad (55)$$

and linearizing Eq. (49) with respect to $v(x, t)$. Choosing the ansatz $v(x, t) = G_1 e^{\sigma t + iKx} + G_2^* e^{\sigma^* t - iKx}$ for the resulting linear equation in $v(x, t)$ leads then to two coupled homogeneous equations for the amplitudes G_1 and G_2 , where K denotes the wave number of the perturbations. The solubility condition for these two equations provides a quadratic polynomial for $\sigma(q, K, b, c)$ and from the neutral stability condition $\text{Re}(\sigma) = 0$, the stability boundaries are determined. In the limit of long-wavelength modulations $K \ll 1$, traveling waves as given by Eq. (53) together with Eq. (54) are stable for wave numbers q that are smaller than the wave number at the Eckhaus stability limit q_E (see e.g. Ref. [47] and references therein) given by

$$q^2 < q_E^2 = \frac{\varepsilon_E}{\xi_0^2} \frac{1 + bc}{3 + bc + 2c^2}. \quad (56)$$

The neutral curve $\varepsilon_N(q)$ and the Eckhaus stability boundary $\varepsilon_E(q)$ are shown in Fig. 4 for one set of parameters of model I. The dashed line in this figure describes the parabolic neutral curve $\varepsilon_N = \xi_0^2 q^2$ as obtained from the amplitude equation (49), whereas the dotted line displays the neutral stability curve including higher order contributions with respect to the wave number q as obtained by solving the fully linear stability problem in Eq. (35). According to this figure, the neutral curves obtained by these two different approaches are in good agreement even beyond the threshold c_{0c} . Inside the dark region delimited by q_E , traveling wave solutions as given by Eqs. (53) and (54) are stable. According to the $\pm q$ symmetry of F and Ω , left or right traveling waves may occur, as discussed in Sec. VI.

However, for values of the coefficients b and c that fulfill the constraint [48, 49]

$$bc < -1 \quad (\text{Benjamin - Feir resonance}), \quad (57)$$

there is no range of wave numbers q where the nonlinear solutions in Eq. (53) are stable. Instead of traveling waves or other stable coherent structures, spatiotemporal chaotic solutions of Eq. (49) are preferred in this case.

For model I and for two different velocity ratios β , the dependence of b and c on the regeneration rate α is shown in Fig. 3, while the product bc is shown in Fig. 5 for two different nucleation rates ν . As indicated by this figure, there exists a specific value α_{BF} of the regeneration rate α below which $bc + 1$ is negative. Traveling waves are therefore unstable in this parameter range of model I.

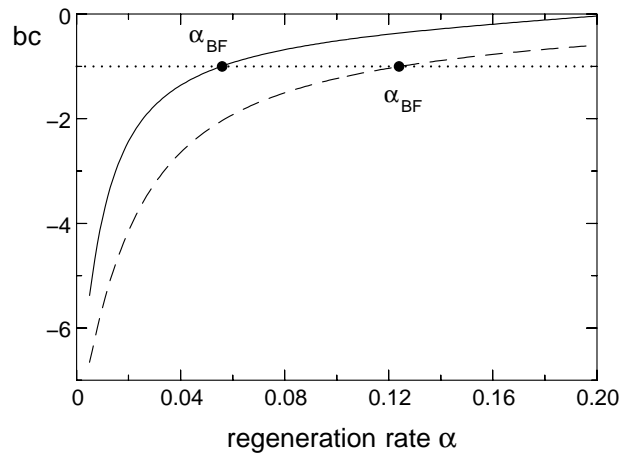


FIG. 5: The product bc as obtained from model I is shown as a function of the regeneration rate and for two different nucleation rates: $\nu = 0.01$ (solid line) and $\nu = 0.05$ (dashed line). The rate α_{BF} is determined by the condition $bc = -1$, which is indicated by the dotted line. Above α_{BF} there exists a finite wave number band $q < q_E$ in which traveling waves are stable, illustrated also as shaded area in Fig. 4. Rest of parameters are $v_g = 0.1, \beta = 0.1, D_c = 0.01$, and $D_p = 0$.

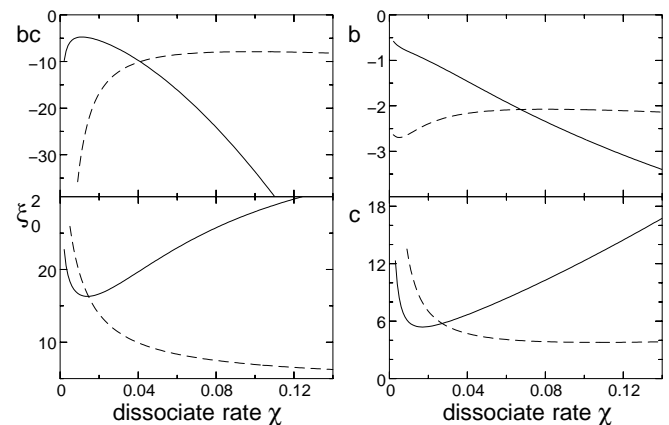


FIG. 6: The linear coefficients ξ_0^2, b and the nonlinear coefficient c of the amplitude equation (49) as well as the product bc are shown for model II as functions of the dissociate rate χ and for $\alpha = 0.01$ (solid line) and $\alpha = 0.1$ (dashed line). For the rest of the parameters, the values $G = 3000, v_g = 0.1, \nu = 0.01, D_c = 0.1, D_{oli} = 0.01$, and $D_p = 0$ have been chosen.

However, the product bc increases with increasing regeneration rates and above the specific value α_{BF} homogeneous oscillations and traveling waves become stable. This means that for $\alpha > \alpha_{BF}$ a finite range of wave numbers $0 < |q| < q_E$ arises, which is delimited by the Eckhaus stability border described by the expression in Eq. (56). This range is also illustrated as shadowed area in Fig. 4. Unlike model I where we always find stable traveling waves for larger values of α , traveling waves are unstable for model II for all parameters we have investi-

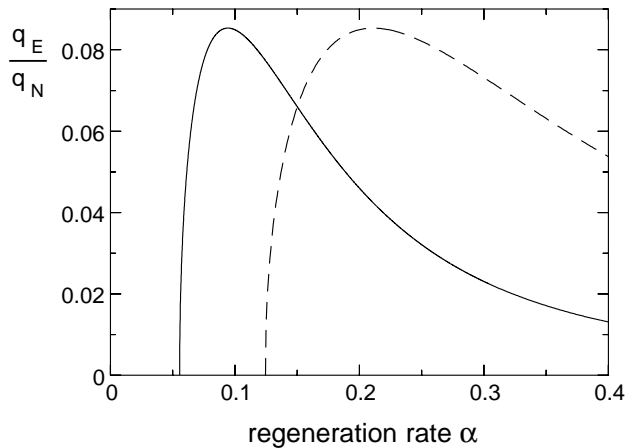


FIG. 7: The wave number ratio q_E/q_N is shown as a function of the regeneration rate α and for two different nucleation rates: $\nu = 0.01$ (solid line) and $\nu = 0.05$ (dashed line). The other parameters are the same as in Fig. 5.

gated. That is, one always has $bc + 1 < 0$ as shown, for instance, in Fig. 6 as a function of χ and for two different regeneration rates α .

For $\alpha > \alpha_{BF}$ in Fig. 5 one has a finite wave number band $-q_E < q < q_E$, where traveling wave solutions are stable. The location of the neutral curve q_N and of the Eckhaus curve q_E changes as a function of the parameters, but the interesting quantity is the portion q_E/q_N of the stable wave numbers within the neutral curve. Accordingly, the dependence of q_E/q_N on the regeneration rate α is shown in Fig. 7 for model I. The width of stable wave numbers is rather small and tends to even smaller values for large values of α .

The expression $bc + 1$ changes according to Fig. 5 its sign for different values of the nucleation rate at different values of α_{BF} . The border line in the $\alpha - \nu$ plane that separates the parameter range of stable traveling waves from that of unstable ones is a further compressed representation of stability, which is shown in Fig. 8 for three different values of the ratio $\beta = v_g/v_s$ between the growth and shrinking velocity of model I. From this figure a few trends can be easily identified: large values of the ratio β or rather small values of the nucleation rate ν enlarge the range of stable traveling waves, whereas small values of the regeneration rate α promote a chaotic solution behavior. Moreover, for parameter combinations of α and ν , where the polymerization cycle nearly comes to a standstill because a great number of tubulin dimers is either incorporated into microtubules, i.e. for large values of ν , or captured in their inactive tubulin- d form, i.e. for small values of α , the preferred solution of the microtubule polymerization cycle is spatiotemporal chaos.

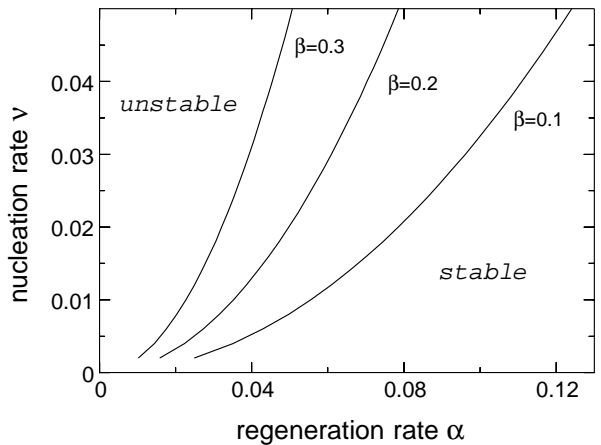


FIG. 8: The border line separating the range where traveling waves are unstable from the range where they are stable in a finite wave number band $q < q_E$ is shown in the plane of the nucleation and regeneration rate for three different values of $\beta = v_g/v_s$. The border lines are determined by the constraint $bc = -1$. In the range of unstable traveling waves, spatiotemporal chaotic solutions are favored. The parameters $v_s = 1$, $D_c = 0.01$, and $D_p = 0$ have been chosen.

VI. NUMERICAL SIMULATIONS OF NONLINEAR SOLUTIONS

In this section the nonlinear solutions of the basic equations for model I and model II as well as of the respective amplitude equation are explored. The validity range of the amplitude equation is estimated by comparing its solutions with those of the full basic equations. For the spatially homogeneous case, we have determined the validity range of the amplitude equation in Ref. [20] by comparing just the oscillation amplitudes obtained from both approaches. For the more general case with spatial degrees of freedom, an additional criterion is employed. Beyond the Hopf bifurcation, we find a boundary in parameter space that separates the range where regular solutions are stable from that where they are linearly unstable. In the linearly unstable range spatiotemporal chaotic solutions are predicted by the amplitude equation approach. However, it may happen that the regular solutions of the basic model equations are still stable in this range, which is then beyond the validity range of the amplitude equation.

The coupled differential equations for the reaction cycle are solved by a numerical scheme proposed already in Ref. [20]. Within this algorithm the dependence of the densities p_g and p_s on the length variable l is approximated, which reduces the computational time also in spatially extended systems considerably, as outlined for model II in the Appendix. For spatially periodic boundary conditions, the partial differential equations are efficiently solved by a pseudo-spectral code, where the conservation of the total amount of tubulin dimers is given by a fixed value of the spatially homogeneous Fourier-

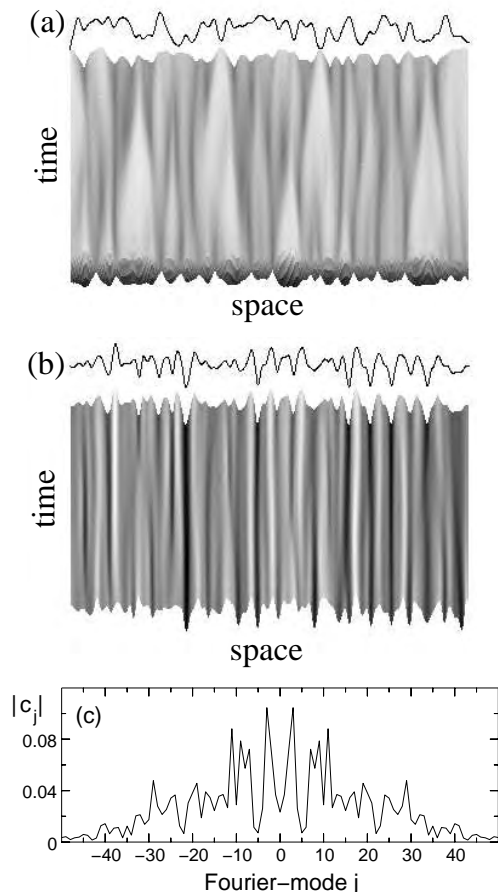


FIG. 9: For model I the spatiotemporal evolution of $c_t(x, t)$ is shown in part (a) and that of $n(x, t)$ in part (b) at $\varepsilon = 0.005$ and for parameter values giving the product $bc = -1.1082$ of the coefficients b and c of the amplitude equation (49). The solutions are shown for a temporal range of $t = 120000$, where the initial range of about $t \approx 10^6$, after starting the simulation with random initial conditions, has been discarded. Part (c) displays the spatial Fourier spectrum of the final state of c_t given in (a). The system length is $S = 512\pi$ and the further parameters are $\beta = 0.1, \nu = 0.01, \alpha = 0.05, D_c = 0.01$ and $D_p = 0$.

mode $\tilde{n}(q = 0, t)$, as explained in the Appendix too.

A. Model I

In Fig. 9(a) we show the spatiotemporal behavior of the tubulin- t concentration $c_t(x, t)$ and in Fig. 9(b) that of the local tubulin concentration $n(x, t)$. Both fields are obtained from numerical simulations of the basic equations of model I for parameters which correspond to the product $bc = -1.1082$ in terms of the two parameters b and c in the amplitude equation (49). According to Fig. 5, this value of the product bc corresponds to a regeneration rate $\alpha < \alpha_{BF}$ and thus, one expects close to the threshold, due to the stability analysis in terms of the

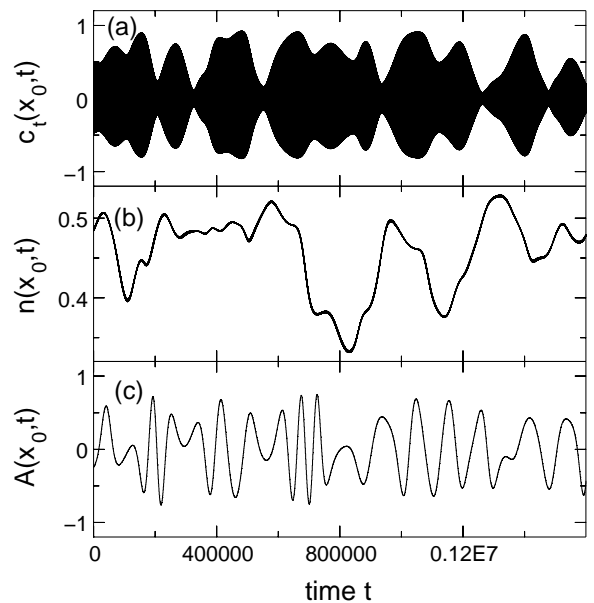


FIG. 10: The temporal evolution of $c_t(x_0, t)$ and $n(x_0, t)$ at a fixed point x_0 is shown in part (a) and (b), respectively, for the same set of parameters as in Fig. 9. The stationary and spatially uniform contribution to c_t and n is not depicted. In part (c) the temporal evolution of the envelope $A(x_0, t)$ of $c_t(x_0, t)$ is shown as obtained by a numerical solution of Eq. (49).

amplitude equation, unstable traveling waves and therefore spatiotemporal chaotic solutions. Indeed, the solutions of the basic equations of model I show in the long run also an irregular spatiotemporal behavior as shown in Fig. 9(a). The time dependence of $c_t(x, t)$ is actually proportional to the periodic function $e^{i\omega_c t}$ with the Hopf frequency ω_c . This rapid oscillation smears out the slow temporal behavior of the envelope, as can be seen by comparing the space-time plot in Fig. 9(a) with that of the envelope $\text{Re}[A(x, t)]$ shown in Fig. 11(a). The very different time scale of the rapid variation proportional to $e^{i\omega_c t}$ and that of the slow variation of the envelope of $c_t(x_0, t)$ can be seen in Fig. 10(a) at a fixed spatial site x_0 , where the fast variation is not resolved anymore. For the same parameters the temporal variation of the time evolution of $n(x_0, t)$ and that of the amplitude $A(x, t)$ are shown in Fig. 10(b) and Fig. 10(c), respectively, and they take place at a similar slow time scale. We should like to point out that the stationary and spatially homogeneous portion of the fields c_t and n is not included in Fig. 10. This representation of the solutions allows a direct comparison with the solutions of the amplitude equation. The tubulin- d concentration, $c_d(x, t)$, as well as the total amount of polymerized tubulin dimers $\gamma L(x, t)$, cf. Eq. (13), are in a similar manner irregular as $c_t(x, t)$ in Fig. 9(a).

Interestingly, at any site x_0 the relative phase between the densities $L(x, t)$, $c_t(x, t)$ and $c_d(x, t)$ of model I is

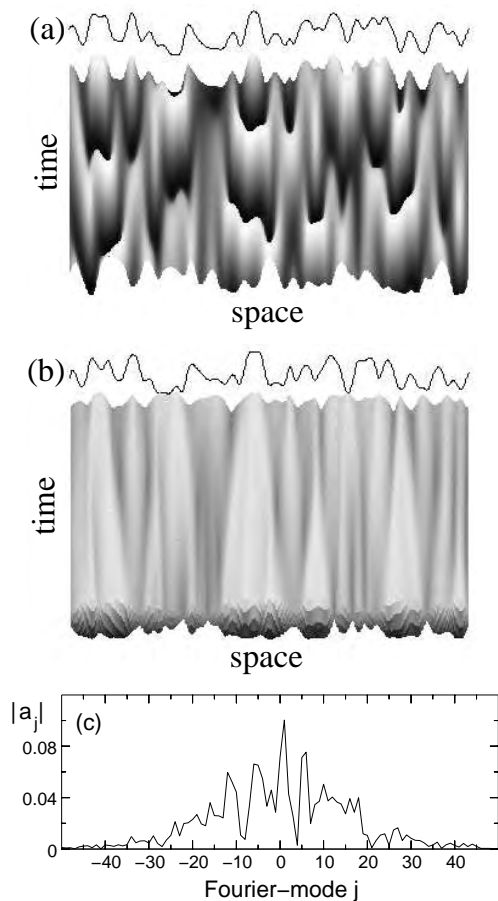


FIG. 11: The spatiotemporal evolution of the solution of the amplitude equation is shown for the same parameters as in Fig. 9. Part (a) displays the time evolution of $\text{Re}[A(x, t)]$ and part (b) that of $\text{Re}[A(x, t) \exp(i\omega_c t)]$, where the frequency ω_c is given at the threshold of the Hopf bifurcation of model I. Part (c) displays the spatial power spectrum of the final state in (a). The shown time window is the same as in Fig. 9.

approximately in accordance with the phase relation between them in the case of purely homogeneous oscillations as described in Ref. [20]. This is due to the underlying closed reaction cycle and the temporally irregular behavior takes place on a time scale being much larger than the time scale ω_c^{-1} of the fast oscillations. These slowly varying contributions are described by the envelope of the oscillating solutions of the polymerization cycle and are illustrated in Fig. 11(a). This figure displays a space–time plot of the envelope of the tubulin- t density $c_t(x, t)$, cf. Eq. (28), as obtained from a numerical simulation of the amplitude equation (49) for the same parameters as in Fig. 9(a). The temporal evolution as shown in Fig. 11(a) and in Fig. 9(a) differs optically due to the fast temporal oscillations of the full solution, which have been removed during the derivation of the amplitude equation. For completeness, the temporal evolution $\text{Re}[A(x, t) \exp(i\omega_c t)]$ is displayed in Fig. 11(b) in order to show the similarities with the full solution $c_t(x, t)$ in Fig. 9(a). At a fixed

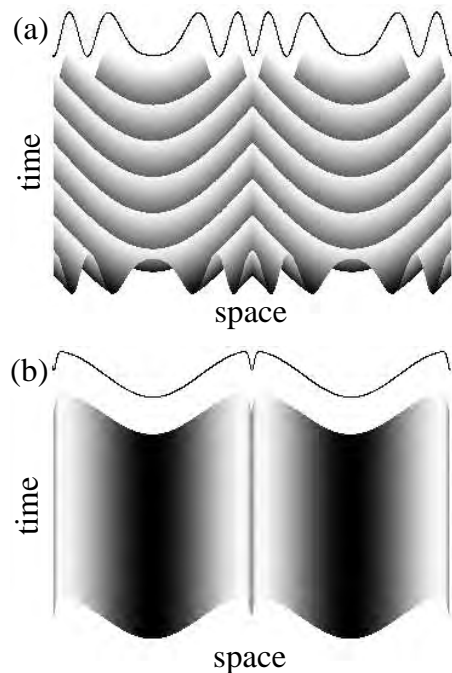


FIG. 12: Spatially anharmonic solutions of model I are shown in part (a) for $c_t(x, t)$ and in part (b) for $n(x, t)$ as they occur at $\varepsilon = 0.03$. They evolve during a long transient period to spatially homogeneous oscillations. By decreasing the control parameter to $\varepsilon = 0.005$, this state terminates in a spatiotemporal chaotic one (see Fig. 9), as predicted on the basis of the amplitude equation for the value $bc = -1.1082$. The shown time interval is $t = 800$ and the other parameters are the same as in Fig. 9.

spatial point x_0 , the envelope of the full solutions of the reaction cycle and the solution of the amplitude equation have a similar complex behavior, which can be seen by comparing the envelope of $c_t(x_0, t)$ in Fig. 10(a) with $A(x_0, t)$ in Fig. 10(c). The dynamics of $A(x_0, t)$ and that of the envelope of $c_t(x_0, t)$ takes place on a comparable time scale that is nearly given by $\tau_0/\varepsilon \approx 30000$. The typical length scale $\xi_0/\varepsilon^{1/2} \approx 14$ of the variations of the envelope $A(x)$ in Fig. 11 is also roughly the same as for $c_t(x)$ or $n(x)$ in Fig. 9. Furthermore, taking for a system of length S the Fourier decomposition of the full solution $c_t(x, t) = \sum_j c_j \exp(i2\pi jx/S)$ and that of the solution of the amplitude equation $A(x, t) = \sum_j a_j \exp(i2\pi jx/S)$, the similarities between both fields can be recognized by comparing Fig. 9(c) with Fig. 11(c). The weights of the Fourier modes are quite similar for both approaches, and the spectra exhibit a rather broad distribution indicating their spatiotemporal irregular character.

Surprisingly, one finds for increasing values of the control parameter ε in the parameter range $bc < -1$ (or $\alpha < \alpha_{BF}$) instead of spatiotemporal chaotic solutions rather regular solutions. A snapshot of such a regular solution is shown for $c_t(x, t_0)$ in the top part of Fig. 12(a) (solid line) for $\varepsilon = 0.03$. The spatiotemporal behavior

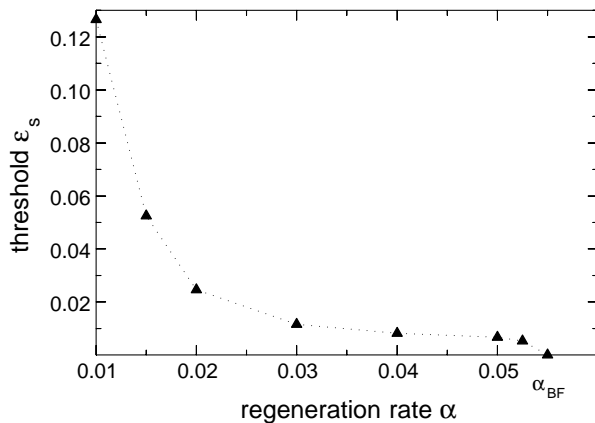


FIG. 13: The secondary threshold $\varepsilon_s(\alpha)$ is shown as it occurs for model I in the range $\alpha < \alpha_{BF}$. Below this curve and beyond the threshold c_{0c} (corresponding to $\varepsilon = 0$), one has spatiotemporal chaos and above the curve homogeneous oscillations. The data points are obtained by starting the simulations with random initial conditions. The dotted line is a guide to the eye. The same parameters are used as in Fig. 5 and $\nu = 0.01$.

of the tubulin- t concentration is described by a superposition of standing waves - $c_t(x, t) \propto \cos(\omega_c t) \cos(2qx) + \cos(\omega_c t + \varphi) \cos(4qx) +$ higher harmonics. The first contribution of c_t is in agreement with the linear solution at threshold given in Eq. (43) and the second contribution as well as higher harmonic terms are due to nonlinear effects. Such solutions may be obtained with spatially periodic starting solutions. However, after a long transient stage these surprising patterns decay to spatially homogeneous oscillations, which are stable beyond a secondary threshold as indicated in Fig. 13. The transient range lasts up to 20 – 30 diffusion times $\tau = (D_c q^2)^{-1}$, where q is the (smallest) wave number of the pattern. Here τ is an appropriate time scale in order to estimate the transient regime.

Starting the simulations directly with a homogeneously oscillating polymerization as initial condition and reducing the control parameter below the secondary threshold, the spatially homogeneous oscillations become unstable and evolve into spatiotemporal chaotic solutions.

Another scenario for the determination of the secondary threshold ε_s is as follows. One may start the simulations with small amplitude random functions and at different values for ε . For $bc < -1$ and close to the threshold of the Hopf bifurcation, the solutions evolve to spatiotemporal chaotic states. However, increasing the control parameter ε beyond the secondary threshold, the simulations terminate after a long transient regime in spatially homogeneous oscillations.

The behavior of $n(x, t)$ in Fig. 12(b) is quite different and nearly stationary. Here the oscillations take place on a very small time scale $\sim 10^{-3}$, which is not resolved in Fig. 12(b). Interestingly, the spatial profile of $n(x, t)$ has some localized dips where the left and right travel-

ing parts of c_t collide. Such a spatially inhomogeneous distribution of the local tubulin density $n(x, t)$ is crucial in order to observe a dynamical behavior for c_t as shown in part (a) or for the other densities c_d and γL of the reaction cycle.

During the transient regime the patterns in Fig. 12 become unstable against inhomogeneous perturbations, when decreasing the control parameter to $\varepsilon = 0.005 < \varepsilon_s$. Eventually they evolve to chaotic states similar to those shown in Fig. 9. Such a destabilization of regular patterns into spatiotemporal chaotic states by approaching the threshold of the Hopf bifurcation from above is not captured by the amplitude equation (49) and the phenomenon is therefore beyond the validity range of the amplitude equation. Accordingly, ε_s marks an upper limit of the validity range of the amplitude equation which depends on the details of the system, such as rate constants, etc.

The secondary threshold occurs in the parameter range where spatiotemporal chaotic states are preferred immediately above threshold. Therefore, one expects that this secondary threshold tends to the threshold of the Hopf bifurcation, when the product bc approaches as a function of α the stability boundary $bc = -1$ in Fig. 5, which corresponds to α_{BF} . Indeed, ε_s tends to the threshold of the homogeneous Hopf bifurcation when $bc \rightarrow -1$ and hence $\alpha \rightarrow \alpha_{BF}$ is approached from below as shown in Fig. 13. This phase diagram subdivides for regeneration rates $\alpha < \alpha_{BF}$ the ε - α plane into regions, where either chaotic or regular structures may be expected beyond the Hopf bifurcation.

If the simulations are started with random initial solutions in the range $\varepsilon > \varepsilon_s$, one first obtains extremely anharmonic patterns. In particular, the spatial profile of the tubulin density $n(x, t)$ has several pronounced dips between them the other densities behave like a superposition of standing waves having great similarity with c_t in Fig. 12(a). Unlike Fig. 12(b), these dips are however not stationary and a kind of coarsening to large scale structures is found, where, for instance, two closely adjacent dips of $n(x, t)$ merge into each other in the course of time. This coarsening process is rather fast and takes place on the time scale $2-3\tau$, whereas the emerging long-wavelength structures persist as long transients before the simulations settle down to spatially homogeneous oscillations.

For regeneration rates $\alpha > \alpha_{BF}$, one obtains either spatially homogeneous oscillations or spatially anharmonic solutions looking like those in Fig. 12. Again, the anharmonic structures are rather long living transients (on the average $20-30\tau$) and one has in long time simulations a smooth transition to spatially homogeneous oscillations. Close to the threshold, a direct transition from the stationary reaction cycle into regularly oscillating solutions is found, being consistent with the stability properties given on the basis of the amplitude equation in Sec. V.

There is the remarkable point that we never found

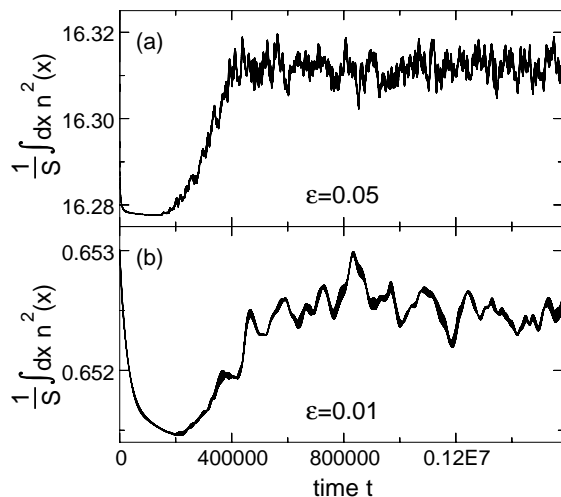


FIG. 14: The temporal behavior of the spatially averaged quantity $N(t) = \frac{1}{S} \int dx n^2(x, t)$ is plotted for two different values of the control parameter ε . Random initial conditions have been used. The regeneration rate is $\alpha = 0.01$ (cf. also Fig. 13) and the remaining parameters are given in the caption of Fig. 9.

traveling wave solutions for the basic equations in the range $\alpha > \alpha_{BF}$, although we may expect them according to the analysis of the amplitude equation. Whenever we started with wave numbers $q < q_E$, we always observed a dynamical behavior as shown in Fig. 12, which only occurs as a transient on the route to spatially homogeneous oscillations. Possibly the wave number band of stable traveling waves in terms of the full equations is smaller than that in terms of the amplitude equation.

Instead of studying the temporal dynamics of the solutions at fixed points in space in order to characterize their spatiotemporal behavior, one may also consider spatially averaged quantities such as $N(t) = 1/S \int dx n^2(x, t)$. For spatially homogeneous oscillations this quantity is constant. In Fig. 14 the temporal evolution of $N(t)$ is shown for two different values $\varepsilon = 0.01, 0.05$ of the control parameter below the secondary threshold and for the regeneration rate $\alpha = 0.01 < \alpha_{BF}$ (cf. Fig. 13). Remaining parameters are the same as in Fig. 9. In both cases the simulations have been started with random functions as initial conditions. Beyond a transient of about $t \approx 400000$, $N(t)$ fluctuates around a certain mean value, which corresponds to the initial concentration of tubulin dimers. Two tendencies can be recognized for increasing values of ε . Firstly, the amplitude of the contributions proportional to $\exp(i\omega t)$ increases with the relative distance ε to the threshold or, equivalent, with the initial tubulin density $c_0 = c_{0c}(1 + \varepsilon)$. Secondly, for $\varepsilon = 0.05$ the time dependence of $N(t)$ includes strong high frequency contributions. This is due to the stronger excitation of higher harmonics and due to the smaller coherence length at larger values of ε . Because of the latter, the temporal dynamics is spatially less correlated than at smaller

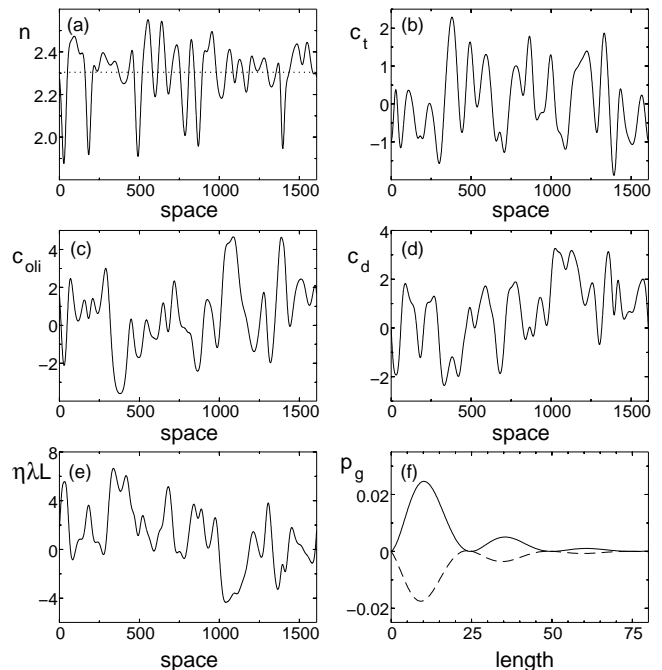


FIG. 15: Spatial profiles of the densities n, c_t, c_{oli} and c_d of model II are shown in parts (a)–(d). Part (e) depicts the spatial distribution of the total amount of polymerized tubulin, described by L in Eq. (17). All solutions are obtained after a simulation time of $t \approx 10^6$. The length distribution of the growing filaments $p_g(l, x_0)$ is shown in part (f) at two fixed space points, where $\eta\lambda L$ in part (e) takes its maximum (solid line) and minimum (dashed line) being located at $x_0 \approx 337$ and $x_0 \approx 1040$, respectively. In all parts the stationary, uniform portion of the respective field is not included (see Appendix). Parameters are $v_g = 0.1, \nu = 0.01, \alpha = 0.01, \chi = 0.02, D_c = 0.1, D_{oli} = 0.01, D_p = 0, \varepsilon = 0.04$ and $L = 512\pi$.

values of ε leading to higher frequency contributions to the spatially averaged quantity $N(t)$. In contrast to this is the behavior of $N(t)$ at small ε . Here the dynamics is extremely slow and the envelope of the basic oscillations hardly varies within a time interval of some multiples of ω_c^{-1} .

B. Model II

For model II, where the dynamics of oligomers instead of shrinking microtubules has been taken into account, one obtains on the level of the amplitude equation for all parameters the inequality $bc + 1 < 0$, as illustrated in Fig. 6. Under this condition homogeneous oscillatory solutions of the amplitude equation are always linearly unstable and one obtains immediately above the Hopf bifurcation spatiotemporal chaotic solutions. In order to verify this prediction of unstable homogeneous solutions also for the basic equations of model II, we performed extensive simulations along the curves $bc(\chi)$ in Fig. 6 by using random initial conditions. In fact, im-

mediately above the threshold of the Hopf bifurcation, one also finds spatiotemporal chaotic solutions. Similar to model I, beyond a secondary threshold ε_s , either long lived spatially anharmonic solutions resembling those in Fig. 12 for model I or stable homogeneous oscillations are found.

A few selected results of the simulations of model II beyond the Hopf bifurcation and below the secondary threshold are shown in Fig. 15(a)-(e). It displays snapshots of the spatial profiles of the different fields that are obtained after a transient of about $t \approx 10^6$ and for random initial conditions. The stationary and spatially homogeneous contributions of the densities n , c_t , c_d , c_{oli} and L are subtracted. Unlike the other densities of the reaction cycle, $n(x, t)$ is always far from being zero and strongly varies around the mean value $c_{0c}\varepsilon$, indicated as a dotted line in part (a), which is conserved in the system.

At the threshold of the homogeneous Hopf bifurcation, the time-dependent part of the length distribution of the growing microtubules $p_g^{(1)}(l, t)$ is given by Eq. (29a) with $\sigma = i\omega_c$. Beyond the threshold two snapshots of the length distribution $p_g^{(1)}(l, t_0)$ are shown in Fig. 15(f), which are obtained from numerical simulations. Both are taken at two different spatial sites x_0 , where the total amount of polymerized tubulin $\eta\lambda L(x, t)$ in Fig. 15(e) takes its maximum [solid line in Fig. 15(f)] and its minimum (dashed line). The envelope of the length distribution $p_g^{(1)}(l)$ is $\exp(-f_{cat}^{(0)}/v_g l)$ which is modulated by a periodically varying function $\propto \exp(-ikl)$ with the wave number $k = \omega_c/v_g$. The spatiotemporal behavior of the associated amplitudes is in general complex. In the case of uniform, regular oscillations the modulation of the length distribution propagates as a traveling wave $\propto \exp[i(\omega_c t - kl)]$ to larger lengths of the microtubules. This may be seen from the analytical expression for $p_g^{(1)}$ in Eq. (29a). Note that negative (positive) values of $p_g^{(1)}(l)$ indicate a smaller (larger) density of the filaments with respect to the stationary length distribution as given in Eq. (22), being consistent with the minimum (maximum) of $\eta\lambda L$ in part (e).

The typical length and time scales of the solutions displayed in Fig. 15, on which their envelope varies, are well described by $\xi_0/\varepsilon^{1/2}$ and τ_0/ε , respectively. Both quantities are obtained in terms of the amplitude equation (49).

VII. SUMMARY AND CONCLUSION

Two models, which capture the major biochemical reaction steps of microtubule polymerization and which have been investigated previously for a spatially homogeneous polymerization [20], are extended in this work by adding spatial degrees of freedom. During the reaction cycle tubulin dimers are only transferred between a few different states but not consumed. Therefore, we have to ensure in the respective models with spatial degrees of freedom the overall conservation of the tubulin

dimers. This conservation is described by a generalized continuity equation for the local density of tubulin, so that the amount of tubulin dimers changes locally, besides the transfer reactions, also via the local fluxes of microtubules, oligomers, or tubulin- t and tubulin- d dimers.

The spatial degrees of freedom do not change the threshold of the Hopf bifurcation, beyond which the stationary reaction cycle becomes unstable against small oscillatory perturbations [20]. The supercriticality of the Hopf bifurcation is not changed as well. However, spatial degrees of freedom alter in a wide range of parameters the stability properties of the homogeneous oscillatory polymerization with respect to inhomogeneous perturbations.

Close to the threshold of a supercritical bifurcation, the weakly nonlinear behavior of the patterns is determined efficiently in terms of the so-called amplitude expansion. In this range the resulting amplitude equation describes the relevant long-wavelength dynamics of the oscillations and it governs also the stability properties with respect to inhomogeneous perturbations, as shown by comparing its solution behaviour with that of the basic equations.

We find for model I that homogeneous oscillatory solutions are unstable immediately above the threshold in a large parameter range via the well-known Benjamin-Feir resonance, this process is terminating in spatiotemporal chaotic solutions. This is the case, for instance, below some critical value α_{BF} of the regeneration rate $\alpha < \alpha_{BF}$. On the other hand, there is for $\alpha > \alpha_{BF}$ a finite range of wave numbers $|q| < q_E$ where traveling waves are stable and the corresponding band of stable wave numbers, the so-called Eckhaus stability band, is given in Fig. 4. For model II we always found for arbitrary parameters immediately above the threshold of the Hopf bifurcation spatiotemporal chaotic solutions.

By numerical simulations of the basic equations, we have also checked, how far beyond the threshold the results of the stability analysis in terms of the amplitude equations are valid. The parameter ranges where the stability results of the amplitude equation can be confirmed have been identified as the validity range of the perturbational approach.

For model I and II the spatiotemporal chaotic behavior, occurring immediately above threshold, is only found below a secondary threshold, beyond which regular oscillating solutions are obtained in numerical simulations starting with random initial solutions. This secondary threshold marks an upper limit of the validity range of the amplitude equations for the presented models. In addition, it may also limit the parameter range of spatiotemporal chaotic solutions in experiments.

Similarly, starting the simulations for control parameters beyond the secondary threshold, the resulting homogeneous oscillations become unstable by decreasing the control parameter and they terminate in irregular, spatiotemporal chaotic states. For model I this rough upper limit of the validity range of the amplitude equation is shown as a function of the regeneration rate in Fig. 13. In the limit $\alpha \rightarrow \alpha_{BF}$ the spatiotempo-

ral chaotic regime vanishes and simultaneously the secondary threshold tends to the primary threshold. Beyond the secondary threshold, also interesting long living anharmonic and transient patterns occur as shown for instance in Fig. 12.

The results concerning our stability analysis of the homogeneously oscillating polymerization hold for two dimensional extended systems as well. On the level of the amplitude approximation, the solutions in two spatial dimensions are well known (see e.g. [47]). In order to explore the two dimensional solution behavior in terms of the basic equations, for instance, beyond the secondary threshold, the numerical scheme presented in the Appendix may be readily extended in future investigations to two spatial dimensions. This also makes an even closer contact to the experimentally observed inhomogeneous oscillatory microtubule polymerization [12]. In our previous work [20] we have shown that for a tubulin concentration below that at the Hopf bifurcation, the oscillatory polymerization takes place only transiently similar as observed in early experiments. Such a behavior corresponds in our spatially extended system to transient patterns.

In a series of experiments surprising gravity-driven patterns have been observed during the microtubule polymerization [21, 51, 52]. How gravity triggers such pattern forming processes is unclear up to now. More recent experiments show that the observed spatially periodic patterns may be related to buckling phenomenon of microtubule bundles [24]. An appropriate extension of the presented models seems to provide a promising approach to these phenomena too.

By increasing the filament density, microtubules may also undergo a transition to an orientational order [42], the so-called nematic order. Such a transition is not included in the present model equations. It has been shown recently that the interplay between the transition to orientational order and a stationary polymerization kinetics may already lead to spatially periodic patterns [31]. Accordingly, the interplay between a transition to orientational order and an ongoing oscillatory polymerization/depolymerization dynamics rises interesting questions as a starting point for inspiring future works.

This work has been supported by a grant from the Deutsche Forschungsgemeinschaft via research unit FOR 608.

APPENDIX: NUMERICAL METHOD FOR MODEL II

The numerical scheme proposed in Ref. [20] for the model equations for a spatially homogeneous microtubule polymerization is extended in this appendix to the models with spatial degrees of freedom as described in Sec. II. For the initial concentration of tubulin dimers, we write $c_0 = c_{0c}(1 + \varepsilon)$ with the relative distance ε to the threshold of the Hopf bifurcation and we present the main steps of the numerical scheme by means of model II.

At first, we choose an ansatz separating the solution of Eq. (1) into its stationary and non-stationary contribution to microtubule polymerization as follows:

$$\begin{aligned} p_g &= p_g^{(0)}(l) + p_g^{(1)}(x, l, t) \\ &= \exp\left(-\frac{f_{cat}^{(0)}}{v_g}l\right) \left(\frac{\nu}{v_g} + F_g(x, l, t)\right). \end{aligned} \quad (\text{A.1})$$

The first and stationary contribution is given by Eq. (22) and the second one covers the time-dependent part as discussed for $\varepsilon = 0$ in Sec. IV B. The ansatz (A.1) leads together with Eq. (1) to a dynamical equation for the time-dependent real function F_g

$$\partial_t F_g = -f_{cat}^{(1)} \left(\frac{\nu}{v_g} + F_g\right) - v_g \partial_l F_g + D_p \partial_x^2 F_g, \quad (\text{A.2})$$

where the catastrophe rate is given by $f_{cat}^{(1)} = f_{cat}^{(0)}[\exp(-c_t^{(1)}/c_f) - 1]$ and $c_t^{(1)}(x, t)$ is the spatiotemporal contribution to $c_t(x, t) = c_t^{(0)} + c_t^{(1)}(x, t)$. A similar separation may be chosen for the other fields $c_d(x, t) = c_d^{(0)} + c_d^{(1)}(x, t)$ and $n(x, t) = n^{(0)} + n^{(1)}(x, t)$ including the stationary parts $c_d^{(0)}$ and $n^{(0)}$. The stationary solutions $p_g^{(0)}, c_t^{(0)}, c_d^{(0)}$ are evaluated at the threshold of the Hopf bifurcation with the associated tubulin density $n^{(0)} = c_{0c}$ while one has the constraint $\frac{1}{S} \int_0^S dx n^{(1)} = c_{0c}\varepsilon$ beyond the Hopf bifurcation.

The l -dependence of the solution $F_g(x, l, t)$ of Eq. (A.2) can be expanded in terms of the first two Fourier modes as follows:

$$F_g = B(x, t) + \frac{1}{2} [C(x, t)e^{ikl} + C^*(x, t)e^{-ikl}]. \quad (\text{A.3})$$

The wave number k is chosen at its threshold value $k = \omega_c/v_g$. Imposing the boundary condition (3) for the growing microtubules leads to $F_g(x, l = 0, t) = 0$ and, therefore, the relation $C_R = -B$ with $\text{Re}(C) = C_R$ follows. The approach in Eq. (A.3) together with Eq. (A.2) yields the relation

$$\text{Im}(C) = C_I = \frac{\nu}{kv_g^2} f_{cat}^{(1)}, \quad (\text{A.4})$$

while the field $B(x, t)$ obeys the following equation of motion

$$\partial_t B = -f_{cat}^{(1)} \left(\frac{\nu}{v_g} + B\right) + D_p \partial_x^2 B. \quad (\text{A.5})$$

Due to the periodically varying contribution to F_g in Eq. (A.3) and due to the envelope of p_g which is exponentially decaying with l in Eq. (A.1), the integrals over the length distribution of the microtubules in Eqs. (10a) and (21) converge and may be readily evaluated in terms of the fields B , C_R and C_I . As a result of these calculations, one obtains the following governing equations for

the densities $c_t^{(1)}$, $c_d^{(1)}$ and $n^{(1)}$

$$\begin{aligned} \partial_t c_t^{(1)} &= -\eta\lambda v_g \frac{k^2 B - \delta k C_I}{\delta(\delta^2 + k^2)} + \alpha c_d^{(1)} \\ &\quad + D_c \partial_x^2 c_t^{(1)}, \end{aligned} \quad (\text{A.6a})$$

$$\begin{aligned} \partial_t c_d^{(1)} &= \chi \left(n^{(1)} - c_t^{(1)} - c_d^{(1)} - \eta\lambda L^{(1)} \right) - \alpha c_d^{(1)} \\ &\quad + D_c \partial_x^2 c_d^{(1)}, \end{aligned} \quad (\text{A.6b})$$

$$\begin{aligned} \partial_t n^{(1)} &= (D_c - D_{oli}) \partial_x^2 (c_t^{(1)} + c_d^{(1)}) + D_{oli} \partial_x^2 n^{(1)} \\ &\quad + (D_p - D_{oli}) \eta\lambda \partial_x^2 L^{(1)}, \end{aligned} \quad (\text{A.6c})$$

where the abbreviation $\delta = f_{cat}^{(0)}/v_g$ has been introduced and where the integrated length of growing microtubules is given by

$$\begin{aligned} L^{(1)}(x, t) &= \int_0^\infty dl l p_g^{(1)}(x, l, t) \\ &= \frac{B(3\delta^2 k^2 + k^4) - 2\delta^3 k C_I}{\delta^2(\delta^2 + k^2)^2}. \end{aligned} \quad (\text{A.7})$$

Assuming spatially periodic boundary conditions for all fields, the set of four partial differential equations, as given by Eq. (A.5) and Eqs. (A.6), may be transformed into Fourier space. The resulting ordinary differential equations with respect to time are integrated numerically by a second-order Runge-Kutta method with a time step $\Delta t = 0.02$.

For the spatially homogeneous part of $n^{(1)}$, one obtains according to Eq. (A.6c) the relation $\partial_t \tilde{n}^{(1)}(q=0, t) = 0$ for the Fourier transform of $n^{(1)}(x, t)$, which is in agreement with Eq. (7). Therefore, $n^{(1)}$ is a conserved quantity with respect to time and its value is fixed by the initial condition $\tilde{n}^{(1)}(q=0, t=0) = c_{0c}\varepsilon$, cf. Eq. (5).

For model I, a similar ansatz as given in Eqs. (A.1) and (A.3) can be made for the shrinking microtubules $p_s(x, l, t)$, which is presented without spatial degrees of freedom in Ref. [20].

-
- [1] B. Alberts, A. Johnson, J. Lewis, M. Raff, K. Roberts, and P. Walter, *Molecular Biology of the Cell* (Garland, New York, 2001).
- [2] H. Lodish, A. Berk, S. L. Zipursky, P. Matsudaira, D. Baltimore, and J. Darnell, *Molecular Cell Biology* (Freeman, New York, 1999).
- [3] J. Howard, *Mechanics of Motor Proteins and the Cytoskeleton* (Sinauer, Sunderland, 2001).
- [4] M. Dogterom, Phys. Rev. Lett. **81**, 485 (1998).
- [5] D. K. Fygenson, E. Braun, and A. Libchaber, Phys. Rev. E **50**, 1579 (1994).
- [6] H. Flyvbjerg, E. Jobs, and S. Leibler, Proc. Natl. Acad. Sci. U.S.A. **93**, 5975 (1996).
- [7] F. Pirolet, D. Job, R. Margolis, and J. Garel, EMBO J. **6**, 3247 (1987).
- [8] M. F. Carlier, R. Melki, D. Pantaloni, T. L. Hill, and Y. Chen, Proc. Natl. Acad. Sci. U.S.A. **84**, 5257 (1987).
- [9] E.-M. Mandelkow, G. Lange, A. Jagla, U. Spann, and E. Mandelkow, EMBO J. **7**, 357 (1988).
- [10] G. Lange, E.-M. Mandelkow, A. Jagla, and E. Mandelkow, Eur. J. Biochem. **178**, 61 (1988).
- [11] R. Melki, M. F. Carlier, and D. Pantaloni, EMBO J. **7**, 2653 (1988).
- [12] E. Mandelkow, E.-M. Mandelkow, H. Hotani, B. Hess, and S. C. Müller, Science **246**, 1291 (1989).
- [13] E.-M. Mandelkow and E. Mandelkow, Cell Motil. Cytoskeleton **22**, 235 (1992).
- [14] Y. Chen and T. L. Hill, Proc. Natl. Acad. Sci. U.S.A. **84**, 8419 (1987).
- [15] M. Dogterom and S. Leibler, Phys. Rev. Lett. **70**, 1347 (1993).
- [16] A. Marx and E. Mandelkow, Eur. Biophys. J. **22**, 405 (1994).
- [17] B. Houchmandzadeh and M. Vallade, Phys. Rev. E **53**, 6320 (1996).
- [18] E. Jobs, D. E. Wolf, and H. Flyvbjerg, Phys. Rev. Lett. **79**, 519 (1997).
- [19] D. Sept, H. J. Limbach, H. Bolterauer, and J. A. Tuszyński, J. Theor. Biol. **197**, 77 (1999).
- [20] M. Hammele and W. Zimmermann, Phys. Rev. E **67**, 021903 (2003).
- [21] J. Tabony and D. Job, Proc. Natl. Acad. Sci. U.S.A. **89**, 6948 (1992).
- [22] J. Tabony, Nanobiol. **4**, 117 (1996).
- [23] J. Tabony, Proc. Natl. Acad. Sci. USA **97**, 8364 (2000).
- [24] Y. Liu and Y. Guo and J. M. Valles and J. X. Tang, Proc. Natl. Acad. Sci. USA **103**, 10654 (2006).
- [25] F. J. Nédélec, T. Surrey, A. C. Maggs, and S. Leibler, Nature **389**, 305 (1997).
- [26] T. Surrey, F. Nédélec, S. Leibler, and E. Karsenti, Science **292**, 116 (2001).
- [27] K. Kruse and F. Jülicher, Phys. Rev. Lett. **85**, 1778 (2000); K. Kruse, J. F. Joanny, F. Jülicher, J. Prost and K. Sekimoto, Phys. Rev. Lett. **92**, 078101 (2004).
- [28] T. Liverpool and M. Marchetti, Phys. Rev. Lett. **90**, 138102 (2003).
- [29] F. Ziebert and W. Zimmermann, Phys. Rev. Lett. **93**, 159802 (2004).
- [30] F. Ziebert and W. Zimmermann, Eur. Phys. J. E **18**, 41 (2005).
- [31] F. Ziebert and W. Zimmermann, Phys. Rev. E **70**, 022902 (2004).
- [32] T. J. Mitchison and M. Kirschner, Nature **312**, 232 (1984).
- [33] T. J. Mitchison and M. Kirschner, Nature **312**, 237 (1984).
- [34] R. A. Walker, E. T. O'Brien, N. K. Pryer, M. F. Soboeiro, W. A. Voter, H. P. Erickson, and E. D. Salmon, J. Cell Biol. **107**, 1437 (1988).
- [35] H. Hotani and T. Horio, Cell Motil. Cytoskeleton **10**, 229 (1988).
- [36] S. Kai, ed., *Pattern Formation in Complex Dissipative Systems* (World Scientific, Singapore, 1992).
- [37] F. H. Busse and L. Kramer, eds., *Nonlinear Evolution*

- of Spatio-Temporal Structures in Dissipative Continuous Systems* (Plenum Press, New York, 1990).
- [38] P. Manneville, *Dissipative Structures and Weak Turbulence* (Academic Press, London, 1990).
- [39] M. C. Cross and P. C. Hohenberg, *Rev. Mod. Phys.* **65**, 851 (1993).
- [40] Y. Kuramoto, *Chemical Oscillations, Waves, and Turbulence* (Springer, Berlin, 1984).
- [41] J. J. Tyson, *The Belousov-Zhabotinskii Reaction* (Springer, Berlin, 1976).
- [42] A. L. Hitt, A. R. Cross, and J. R. C. Williams, *J. Biol. Chem.* **265**, 1639 (1990).
- [43] N. Caudron, O. Valiron, Y. Usson, P. Valiron, and D. Job, *J. Mol. Biol.* **297**, 211 (2000).
- [44] R. Wade, F. Pirollet, R. Margolis, J. Garel, and D. Job, *Biol. Cell* **65**, 37 (1989).
- [45] M. Doi and S. F. Edwards, *The Theory of Polymer Dynamics* (Clarendon, Oxford, 1986).
- [46] O. Valiron, N. Caudron, and D. Job, *Cell. Mol. Life Sci.* **58**, 2069 (2001).
- [47] I. Aranson and L. Kramer, *Rev. Mod. Phys.* **74**, 99 (2002).
- [48] J. T. Stuart and R. C. DiPrima, *Proc. R. Soc. London, Ser. A* **362**, 27 (1978).
- [49] A. C. Newell, in *Lectures in Applied Mathematics* (Amer. Math. Soc., Providence, RI, 1974), vol. 15, p. 157.
- [50] S. H. Strogatz, *Nonlinear Dynamics and Chaos* (Addison-Wesley, New York, 1994).
- [51] J. Tabony and D. Job, *Nature* **346**, 448 (1990).
- [52] J. Tabony, *Science* **264**, 245 (1994).